

Chapter 3

Development of Simultaneous PET/MRI Technology for Robust *In Vivo* Studies

3.1 Further Considerations of PET Insert Effects on *In Vivo* MRI Performance

Initial studies with the MR-compatible PET insert demonstrated good SNR and uniformity of MRI images with little distortion and narrow FWHM values of single-pulse water proton spectra in the presence of the PET [106]. Here, we address aspects of MRI image quality that are relevant for robust *in vivo* studies.

3.1.1 Materials and Methods

3.1.1.1 B_0 Effects within the MR FOV

A glass spherical phantom (diameter = 3 cm) containing water doped with Gd-DTPA (such that the solution had $T_1, T_2 = 200$ ms at 7 T) was placed in a home built birdcage RF coil (ID = 35 mm) positioned in the isocenter of the MRI for all imaging studies. B_0 maps were acquired using the *FieldMap* routine implemented in Paravision 5.1. The routine consists of a 3D double gradient echo dataset acquisition (TR = 20 ms, TE1/TE2 = 1.43/5.43 ms, FA = 20°, Matrix size = 64 × 64 × 64, FOV = 80 × 80 × 80 mm³ centered in the isocenter of the MRI, SNR threshold = 5), followed by a phase difference calculation on the reconstructed datasets, and finally a phase unwrapping and conversion to a B_0 frequency fieldmap. B_0 fieldmaps (and magnitude images) were generated by the *MAPSHIM* macro and converted to units of ppm (assuming 300 MHz at 7 T). B_0 maps were

obtained for three conditions:

1. No PET insert.
2. PET insert in the MRI, unpowered.
3. PET insert in the MRI, powered.

Magnitude images were used to identify voxels which bore real signal in the fieldmaps using a signal intensity threshold. Voxels which had viable spatial ΔB_0 values for all three conditions were compared. ΔB_0 linewidths with and without the PET were plotted against each other and the differences between the conditions calculated.

B_0 fieldmaps were also obtained with and without the presence (powered) of the PET insert for a glass cylindrical phantom (OD = 28 mm, length = 61 mm, volume = 20 mL) containing distilled water doped with $CuSO_4$ ($[CuSO_4] = 1.3$ mM, $T_1 = 440$ ms, $T_2 = 350$ ms at 7 T, *FieldMap* routine: TR = 20 ms, TE1/TE2 = 2/5.81 ms, FA = 20°, matrix size = 177 × 177 × 80, FOV = 35.35 × 35.35 × 60 mm³ centered in the isocenter of the MRI, SNR threshold = 5).

3.1.1.2 B_1 Measurements within the MR FOV

Relative B_1 maps with (powered) and without the presence of the PET insert were acquired using the $CuSO_4$ solution phantom described in section 3.1.1.1. Maps were obtained with an extended multi-flip angle method that accounts for inhomogeneous B_0 and B_1 fields [137]. A series of 21, slab selective, 3D gradient echo images were acquired (TR = 1500 ms, TE = 5 ms, matrix size = 32 × 32 × 16, FOV = 35.35 × 35.35 × 58 mm³, bandwidth = 50 kHz, second phase direction: axial). The reference pulse gain was altered across an attenuation range of 42.6 dB to 3.3 dB. This corresponded with a FA range of 10° to 400° at 20° increments. A relatively short 0.3 ms rectangular RF pulse with FWHM of 4.3 kHz was used to suppress the influence of remaining B_0 inhomogeneities during excitation besides those resulting from the slab excitation gradient. The magnitude signals from the image series were fitted to the following equation:

$$S(I) = \kappa \sqrt{(\sin(\frac{\pi}{2} - \theta(I)) \sin(\alpha(I)))^2 + (\cos(\frac{\pi}{2} - \theta(I)) \sin(\frac{\pi}{2} - \theta(I)) (1 - \cos(\alpha(I))))^2}, \quad (3.1)$$

where I is the coil current applied for each flip angle α , S is the image signal intensity, and κ is a constant term incorporating the proton spin density, coil sensitivity, and geometry. In the presence of field inhomogeneities, excitation of the sample may be off-resonance. For this scenario, the effective excitation field B_{eff} about which magnetization is being rotated is deflected out of the transverse (xy) plane towards B_0 (z plane) and is described by

$$B_{eff} = \frac{1}{\gamma}(\Delta\omega e_z + \omega_1 e_{xy}), \quad (3.2)$$

where ω_1 is the angular frequency of the rotation around the axis of the excitation field in the transverse plane, $\Delta\omega$ is the difference in angular velocity between the Larmor precession about B_0 and the rotation of the excitation field. For a given $\Delta\omega$ and B_{1u} (B_1 per unit current), the angle θ between B_{eff} and the transverse plane is given by

$$\theta(I) = \tan^{-1}\left(\frac{\Delta\omega 2\pi}{B_{1u}I\gamma}\right). \quad (3.3)$$

The actual FA in the presence of off-resonant excitations is

$$\alpha(I) = \tau \sqrt{(\Delta\omega 2\pi)^2 + (B_{1u}I\gamma)^2}. \quad (3.4)$$

τ is the duration of the RF excitation pulse.

The coil current I at different flip angles were not measured for this study. Instead, relative B_{1u} maps with and without the PET insert were compared. Coil current was derived from the nominal FA assuming a B_{1u} field strength of 1 mT/A and using the on-resonance FA equation:

$$\alpha = \gamma\tau B_{1u}I. \quad (3.5)$$

3.1.1.3 T_1 Measurements within the MR FOV

Robust quantitative MRI studies (such as DCE-MRI) require the derivations of quantitative T_1 maps. We evaluated the variations of T_1 measurements due to the presence of the PET insert. A glass cylinder (diameter = 4 mm) filled with Gd-DTPA doped water placed on the side of the animal holder during routine animal studies was used for this evaluation. T_1 maps were calculated using

a variable flip angle method. Gradient echo images (FLASH, FA = 12°, 24°, 36°, 48°, 60°, matrix size = 140 × 80, voxel size = 0.25 × 0.25 mm², slice thickness = 1 mm, 9 slices) were obtained at the center of the MRI with (TR/TE = 400/ 2 ms) the PET insert powered on in the bore and the PET insert removed (TR/TE = 200/2 ms). The TR values were different since the temperature requirements of the PET precluded the use of sequences with short TR. Voxel-by-voxel T_1 maps were derived from ROIs manually drawn at the center slice of each dataset and fitted to

$$S = S_0 \frac{\sin\theta(1 - e^{-TR/T_1})}{(1 - \cos\theta e^{-TR/T_1})}, \quad (3.6)$$

where S is the signal intensity measured from the image. T_1 maps obtained with and without the PET on five separate studies each were analyzed. A nonlinear Levenberg-Marquardt algorithm implemented in MATLAB was used for the data fitting.

3.1.1.4 Signal Drift

Feasibility of simultaneous dynamic PET/MRI was evaluated. A T_1 -weighted DCE-MRI sequence (FLASH, TR/TE = 400/2 ms, FA = 30°, matrix size = 140 × 80, voxel size = 0.25 × 0.25 mm², slice thickness = 1 mm, 11 slices, time resolution = 30 s, 90 repetitions) was run with and without the PET insert installed to image tumor-bearing mice. 0.2 mmol/kg Gd-DTPA was injected via the tail vein into each mouse 5 minutes into each scan. A dynamic R_2^* -weighted sequence (FLASH, TR/TE = 600/8.5 ms, FA = 30°, Matrix size = 128 × 128, Voxel size = 0.2 × 0.2 mm², slice thickness = 0.754 mm, 9 slices, time resolution = 60 s, 200 repetitions) was run with the PET insert installed to image the mouse brain. 20 mg/kg Fe ferumoxytol was injected into each mouse via the tail vein 20 minutes into the scan. Tumor, brain and glass cylinder (filled with olive oil, inner diameter = 1.5 mm) ROIs drawn in the appropriate datasets were used for image analysis. The following parameters [138] were measured:

1. The temporal drift of the mean signal intensity across the rod ROIs. A second-order polynomial to the time series was fitted. The difference between the minimum and maximum of the fitted curve was then determined. The result is expressed as a ratio to the signal mean.
2. Fast temporal fluctuations of the mean signal (root mean squared error, RMSE). The slow

temporal drift of the mean signal from the rod ROIs was first removed. The RMSE was determined from the ratio of the detrended signal SD to overall signal mean.

The parameters was calculated from three separate datasets for each separate condition.

3.1.2 Results

3.1.2.1 B_0 Effects within the MR FOV

ΔB_0 comparison for the spherical phantom with and without the presence of the PET is shown in figure 3.1. Fieldmaps are shown in figure 3.2. No significant difference was observed between the PET powered off and powered on conditions compared to the no PET condition. Linewidth differences (in ppm) were -0.04 ± 0.29 and -0.01 ± 0.32 respectively. Fieldmaps for the cylindrical phantom with and without the PET are shown in figure. $\Delta \Delta B_0$ comparison for this phantom is shown in figure 3.4. The linewidth difference (in ppm) between the PET powered on and no PET condition for this phantom was -0.16 ± 0.36 . For both phantoms, the linewidth remained at <1 ppm within most of the imaging volume with or without the PET insert. This is consistent with the specifications of the manufacturer which state that the main magnetic field has an inhomogeneity <1 ppm in a spherical volume with a diameter of 11 cm.

3.1.2.2 B_1 Measurements within the MR FOV

Relative B_{1u} maps for the cylindrical phantom with and without the PET insert are shown in figure 3.5. A voxel-by-voxel comparison of the B_{1u} values is plotted in figure 3.6. Mean, SD, and CoV of the relative B_{1u} values are shown in table 3.1.

Table 3.1: Relative B_{1u} values with and without the PET insert

Condition	Relative B_{1u} (mT/A)	CoV
No PET installed	0.22 ± 0.03	0.16
PET installed and powered on	0.24 ± 0.03	0.14

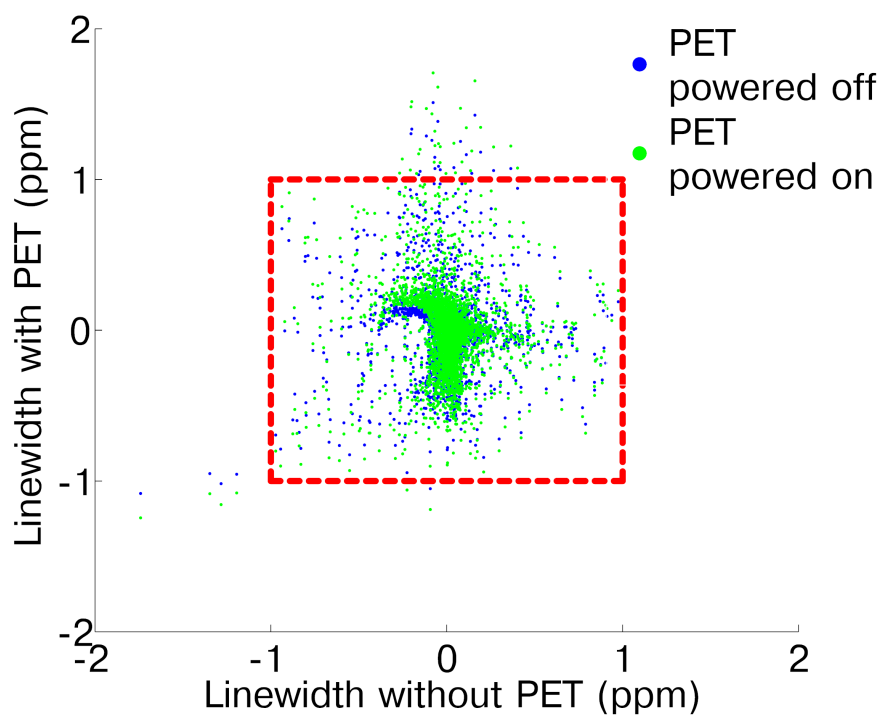
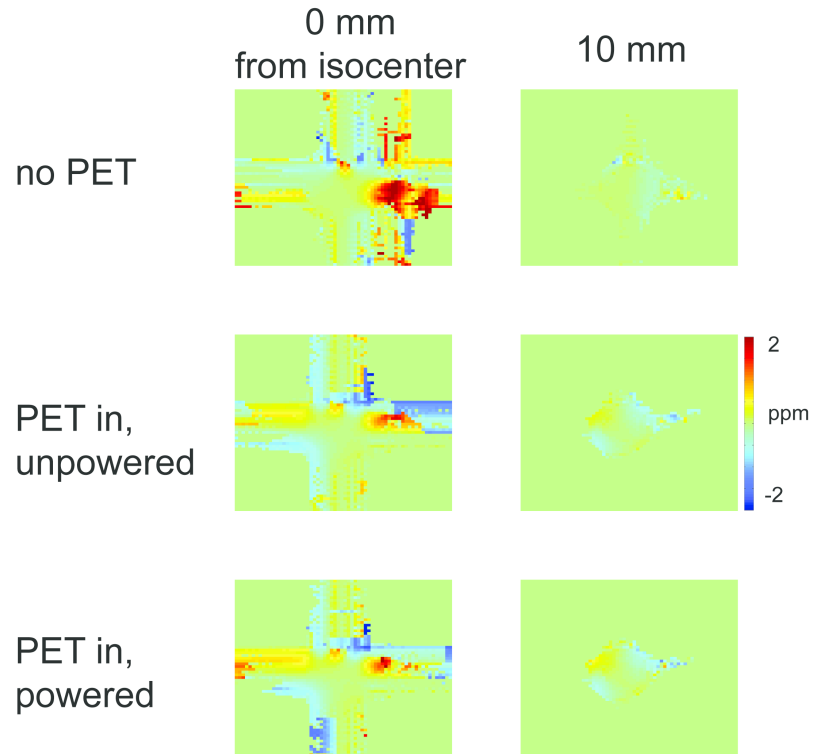
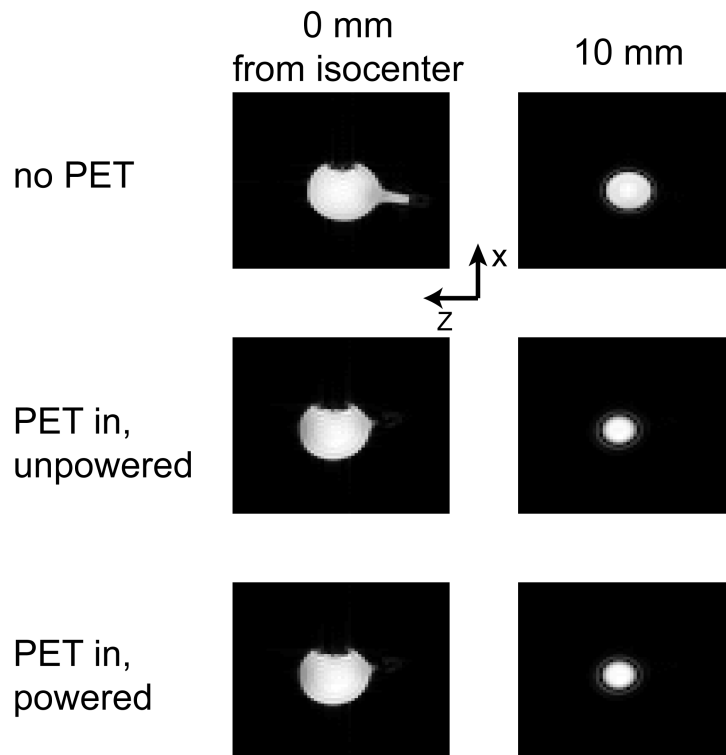


Figure 3.1: B_0 comparisons with and without the PET insert for the spherical phantom. Fieldmap voxels from matching spatial locations in the presence or absence of the PET insert (powered on and off) were compared in a scatter plot. No significant difference in ΔB_0 between the PET on and off conditions were seen. The fieldmap within the MRI imaging volume were within the B_0 inhomogenieties specified by the manufacturer (<1 ppm, defined by the red box) regardless of the presence of the PET insert inside the MRI.

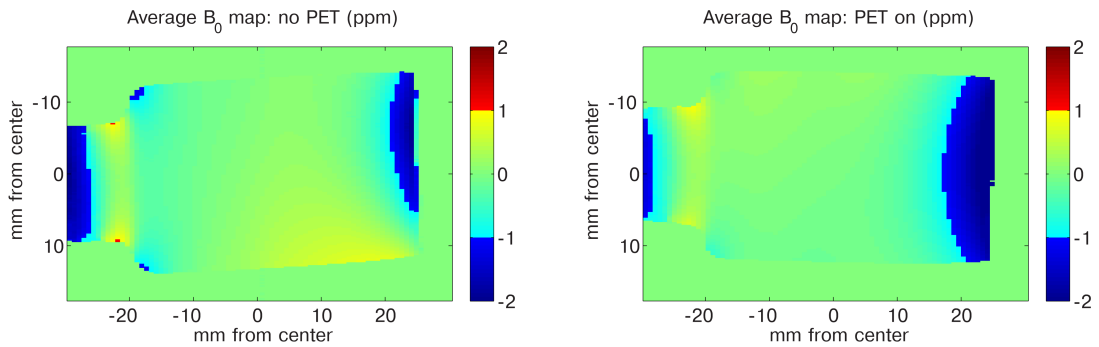


(a) Fieldmaps calculated at the MRI isocenter (left) and 10 mm lateral to the isocenter (right) for different PET insert conditions for the spherical phantom. No significant differences in the fieldmaps were seen in the presence of the PET insert.

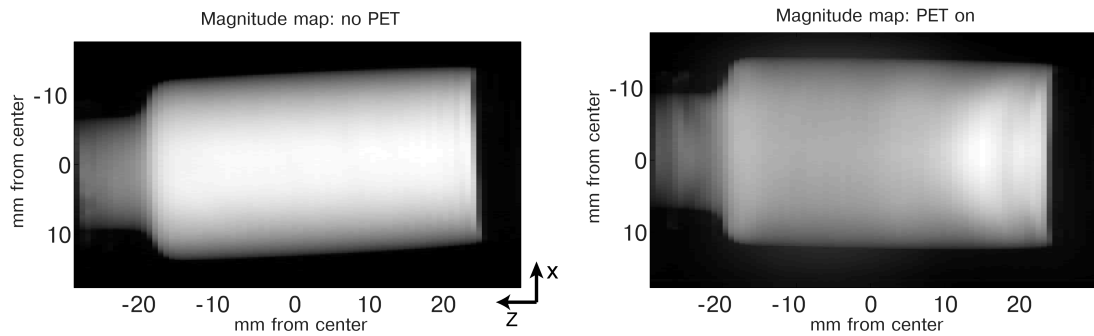


(b) Magnitude images of corresponding fieldmaps shown in (a). Slices are in sagittal orientation.

Figure 3.2: B_0 fieldmaps in the presence of the PET insert for the spherical phantom.



(a) Fieldmaps calculated for the cylindrical phantom without (left) and with (right) the PET insert. The average linewidth within the phantom were <1 ppm whether the PET was present or not. Inhomogeneities >1 ppm were observed for both conditions at outer edges of the phantom, corresponding to the cap and the bottom surface.



(b) Magnitude images of corresponding fieldmaps shown in (a). Slices are in sagittal orientation.

Figure 3.3: B_0 fieldmaps in the presence of the PET insert for the cylindrical phantom.

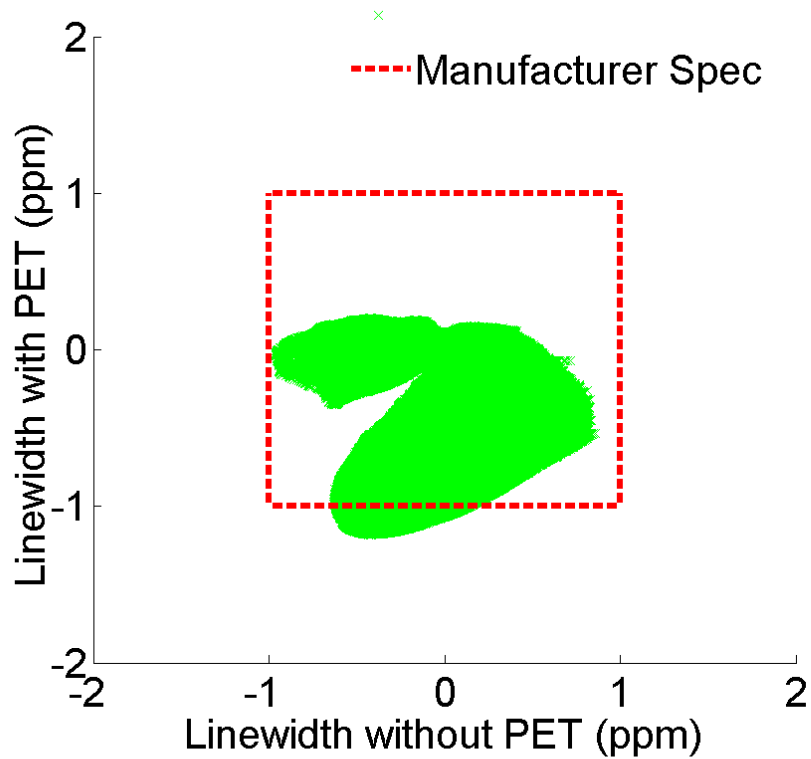


Figure 3.4: B_0 comparisons with and without the PET insert for the cylindrical phantom. Fieldmap voxels from matching spatial locations in the presence or absence of the PET insert (powered on), within the central 30 mm of the MR FOV (along the axial direction), were compared in a scatter plot. No significant difference in ΔB_0 between the PET on and off conditions were seen. The fieldmap within the MRI imaging volume were mostly within the B_0 inhomogeneities specified by the manufacturer (<1 ppm, defined by the red box) regardless of the presence of the PET insert inside the MRI. A small group of voxels lying outside the 1 ppm threshold corresponds with the bottom glass surface of the phantom (figure 3.3).

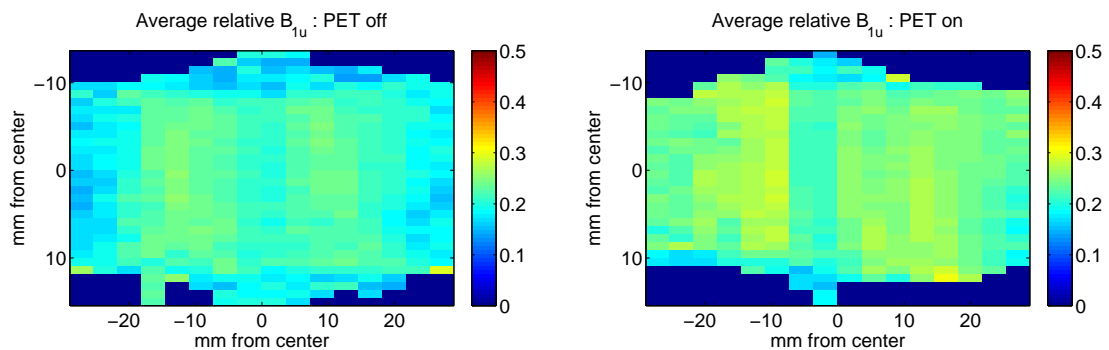


Figure 3.5: Relative B_1 maps with and without the PET insert.

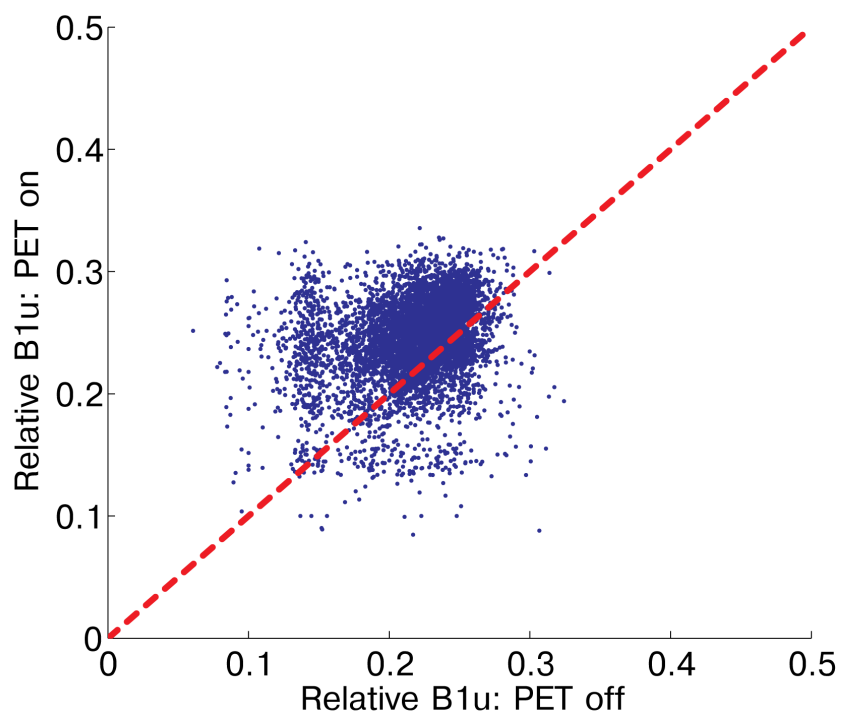


Figure 3.6: B_{1u} comparisons with and without the PET insert for the cylindrical phantom. Fieldmap voxels from matching spatial locations in the presence or absence of the PET insert (powered on) were compared in a scatter plot.

3.1.2.3 T_1 measurements within the MR FOV

T_1 rod measurements with and without the PET insert is shown in Table 3.2. The presence of the PET insert resulted in a slight increase of the mean and SD of T_1 values measured from the rod. However, this increase was not significantly different (two-sided t-test, $p = 0.2$).

Table 3.2: T_1 measurements with and without the PET insert

Condition	T_1 (ms)
No PET installed	473±27
PET installed and powered on	552±50

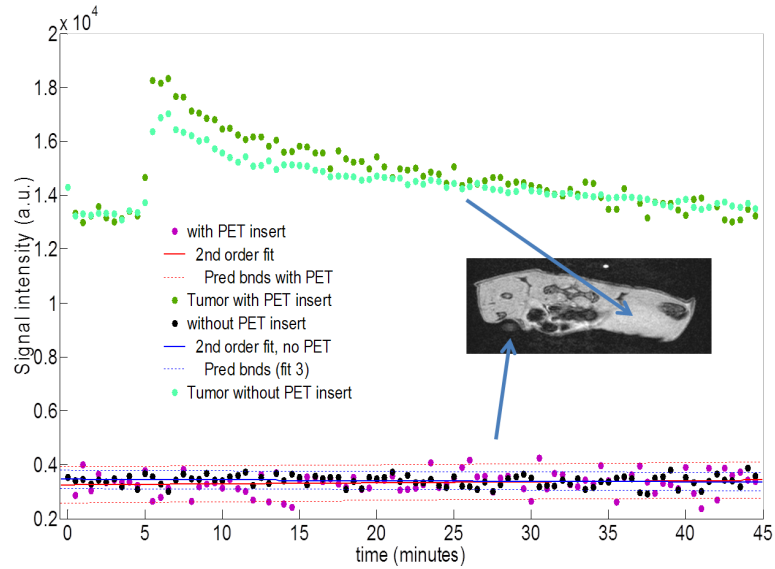
3.1.2.4 Signal Drift

Representative time traces from T_1 - and R_2^* -weighted sequences are shown in figure 3.7. No major signal drift was observed in the presence of the PET insert. Signal changes due to the injection of contrast agents were clearly seen with or without the PET insert. This observation was confirmed from the quantitative signal drift and RMSE metrics (figure 3.8). However, there were small increases in signal drift and RMSE when the PET insert installed; the latter was statistically significant.

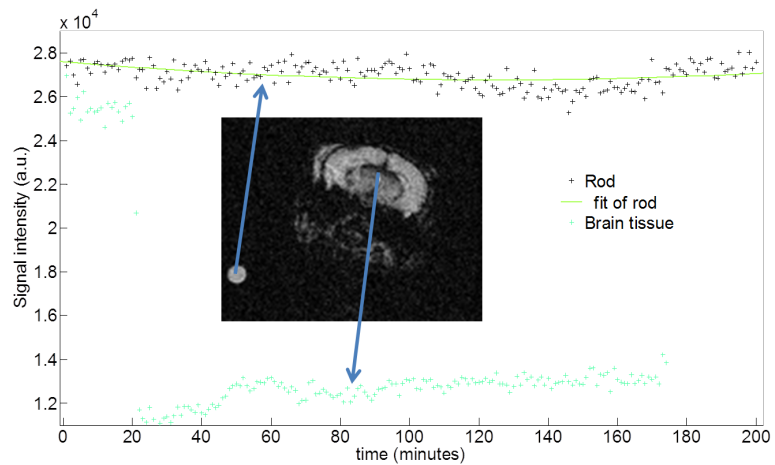
3.1.3 Discussion

Characterization of MRI performance show that ΔB_0 maps did not differ significantly in the presence of the PET insert. Small differences were observed for relative B_{1u} values obtained with and without the PET insert. B_1 inhomogeneity is a recognized issue for quantitative high field (>3 T) MRI [139, 140, 141]. However, this did not result in significant differences of the T_1 values measured during typical PET/MRI study situations. These observations are consistent with studies performed on other hybrid systems [138]. Variation between individual scans can be attributed to multiple factors. The phantoms were removed from the MRI during installation of the PET insert and thus could not be exactly repositioned. The presence of additional shielding material in the bore when the PET is installed may also introduce unwanted eddy currents and reduce SNR [142].

The slight decrease in SNR is reflected in the quantitative measurements of dynamic MR drift.



(a) T_1 -weighted DCE-MRI traces with and without the PET insert. Sudden increase of signal in the tumor corresponds to CA injection (~ 5 minutes into the scan).



(b) R_2^* -weighted time trace with the PET insert installed. Signal decrease in brain at ~ 20 minutes corresponds to injection of iron oxide contrast agent.

Figure 3.7: Dynamic MRI time traces with and without the PET insert.

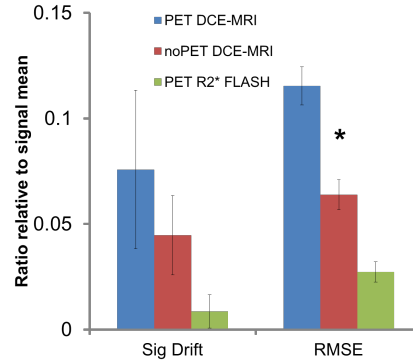


Figure 3.8: Signal drift quantification with and without the PET insert for T_1 - and R_2^* -weighted sequences. A slight increase in both signal drift and RMSE were observed when the PET was installed ($p < 0.05$ for RMSE).

Both signal drift and RMSE increased in the presence of the PET for DCE-MRI datasets. Unlike the drift observed by Wehrl *et al.* [138], these drift increases were not directional and mainly reflect the SNR attenuation in the presence of the PET. They noted that drift in both the PET and MRI signals over time on their system are influenced by temperature fluctuations. We too have observed this phenomenon, and thus utmost care is taken to maintain stable temperature during all our PET/MRI studies.

It is important to note that our drift assessments were performed on an oil-filled rod. The lower SNR of oil, compared to Gd-DTPA and $CuSO_4$ used in other studies, would contribute to the relatively lower drift and RMSE values. Gd-DTPA doped water and a rod with a larger diameter is now used for quality control of the signal drift. Importantly, qualitative assessments of signal changes due to contrast agent (both T_1 and T_2^* agents) injection showed a clear signal trace in *in vivo* tissue with and without the PET. This shows that the dynamic PET/MRI studies we wish to pursue are quite feasible since they all involve contrast agent injection. Further assessment is needed to explore the signal drift without contrast agents (e.g. BOLD studies).

In summary, we have characterized various aspects of the MRI system performance important for robust *in vivo* imaging in the presence of the PET insert. The results suggest that while the presence of the PET insert does affect the quality of MR images produced, the effects are small and should not hinder the acquisition of meaningful *in vivo* simultaneous PET/MRI data.

3.2 A Robust Coregistration Method for *In Vivo* Studies Using a First Generation Simultaneous PET/MRI Scanner

3.2.1 Abstract

3.2.1.1 Purpose

Hybrid positron emission tomography (PET)/magnetic resonance (MR) imaging systems have recently been built that allow functional and anatomical information obtained from PET and MR to be acquired simultaneously. The authors have developed a robust coregistration scheme for a first generation small animal PET/MR imaging system and illustrated the potential of this system to study intratumoral heterogeneity in a mouse model.

3.2.1.2 Methods

An alignment strategy to fuse simultaneously acquired PET and MR data, using the MR imaging gradient coordinate system as the reference basis, was developed. The fidelity of the alignment was evaluated over multiple study sessions. In order to explore its robustness *in vivo*, the alignment strategy was applied to explore the heterogeneity of glucose metabolism in a xenograft tumor model, using ^{18}F -FDG-PET to guide the acquisition of localized ^1H MR spectra within a single imaging session.

3.2.1.3 Results

The alignment method consistently fused the PET/MR datasets with subvoxel accuracy (registration error mean = 0.55 voxels, <0.28 mm); this was independent of location within the field of view. When the system was used to study intratumoral heterogeneity within xenograft tumors, a correlation of high ^{18}F -FDG-PET signal with high choline/creatine ratio was observed.

This section is published in *Medical Physics*: Thomas S. C. Ng, Daniel Procissi, Yibao Wu, and Russell E. Jacobs (2010) A robust coregistration method for *in vivo* studies using a first generation simultaneous PET/MR scanner. *Medical Physics*, 37 (5). pp. 1995–2003.

Acknowledgments: The authors thank Dr. Andrew Raubitschek for providing the mice and tumors, Dr. Scott Fraser, Dr. Simon Cherry, Dr. Jinyi Qi, Dr. Ciprian Catana, and Dr. James Bading for advice on imaging issues and support, Hargun Sohi and Marucha Sanchez for animal handling, Sonia Collazo for computer assistance and Andrey Demyanenko for making the animal RF coil. The project was funded in part by NIBIB Grant No. R01 EB000993, NCRR Grant No. U24 RR021760, Mouse BIRN, a student fellowship from the SNM Education and Research Foundation, and the Beckman Institute.

3.2.1.4 Conclusions

The authors present an implementation of an efficient and robust coregistration scheme for multimodal noninvasive imaging using PET and MR. This setup allows time-sensitive, multimodal studies of physiology to be conducted in an efficient manner.

3.2.2 Introduction

Noninvasive, multimodal imaging is increasingly being adopted for both clinical and preclinical studies, as researchers realize that information available from different image contrasts can complement each other to provide more insights into physiological processes of intact, living animals [143, 144, 58, 145, 146]. The most prominent example of this has been the widespread adoption of combined positron emission tomography (PET) and computed tomography (CT) systems. Anatomical information from the CT has been very useful in giving context to the PET image, especially in oncology research [147, 148, 149, 150]. In both clinical and small animal PET/CT systems, a combination of careful hardware alignment along with image registration via fiducial markers, phantoms, and/or matching of expected uptake patterns in the two images allows accurate spatial fusion of PET and CT images [151, 152, 153, 154].

Magnetic resonance (MR) imaging is another imaging modality widely used for noninvasive, *in vivo* imaging. It can provide high-resolution, soft tissue details, along with functional and metabolic information via techniques such as blood oxygenation level dependent (BOLD) imaging [155], diffusion [156], and spectroscopy [157]. Recognizing the complementary nature of PET and MR information, especially the utility of the information from multimodal images acquired simultaneously [158], researchers have developed hardware for hybrid PET/MR systems. Approaches range from MR-compatible PET systems using avalanche photodiode (APD) technology for simultaneous PET/MR imaging [105, 102], a split magnet that can house current state-of-the-art PET detector systems [94], to field-cycling approaches that allow PET and MR images to be obtained sequentially [159].

As the combined PET/MR technology matures, it is necessary to develop techniques and imaging strategies that maximize the capabilities of such systems to study interesting and novel biological and clinical questions. An important consideration for multimodal systems is a robust method

to merge individual datasets. For small animal PET/CT systems, significant efforts are devoted to ensure good intermodality spatial registration. Two main methods are used: A set of PET and CT visible fiducial markers are imaged with the animal to allow retrospective image registration [151, 154]. Alternatively, a registration transform is defined between the fields of view (FOVs) of the PET and CT scanners through judicious design of PET/CT phantoms that span the FOV of both systems, coupled with a reproducible method to position physically the animal holder in both FOVs [153].

Conceivably, one can adopt similar alignment approaches for PET/MR systems. Two main issues need to be considered specifically in PET/MR systems for spatial alignment purposes. First, the geometry is more constrained in PET/MR than for PET/CT setups. The typical ring diameter for a commercial small animal PET/CT is ~15 cm or greater, compared to 6 cm for the current APD-based PET/MR inserts [102, 160]. The animal subject, radiofrequency (RF) coil, and physiological maintenance and monitoring devices need to fit inside this ring. Moreover, to maximize signal-to-noise ratio (SNR) for MR images, it is often desirable to position the excite/receive RF coils close to the animal. All these factors limit the imaging of fiducial markers concurrently with an animal without specialized invasive approaches [161]. Second, the FOV of the MR is not fixed between scans. An advantage of MR imaging is the flexibility to alter the FOV geometry and resolution of the acquired data depending on the biological region of interest (ROI) within the animal. For example, fMRI BOLD imaging in monkeys and humans often use oblique brain slices to isolate specific functional brain areas; cardiovascular imaging applications may need oblique slices to image structures such as the aortic arch; while dynamic MRI scans may require a tight FOV to obtain sufficient spatial and time resolution. In such cases, we cannot determine the MR imaging FOV *a priori* to facilitate direct PET to MR image alignment. For the purposes of flexible simultaneous PET/MR imaging, we require a reliable strategy to efficiently determine the intersection of the PET and MR FOVs for all scans during the imaging session. Subsequent to the imaging, we also require a method to register the reconstructed PET/MR images to form a multimodal dataset.

In a previous study, Judenhofer *et al.* [102] showed that fusion of individual simultaneous PET and MR phantom images using a rigid body transform is possible using an APD-based PET/MR system, with the registration error on the PET/MR image sets after transformation within the spatial

resolution of the PET system. This suggests that APD-based PET systems produce images that can be aligned consistently to the MR datasets. In this paper, we extend this observation to develop and evaluate an efficient acquisition and processing setup of simultaneously acquired PET/MR data using a position sensitive APD-based, small animal MR-compatible PET insert. The setup ensures robust spatial alignment of the PET and MR images by first aligning the PET FOV and a fixed MR FOV using a PET/MR visible phantom. The registration accuracy of using a single PET to fixed MR FOV registration for the alignment of images from multiple study sessions was then evaluated. Further, we describe an algorithm to relate multiple MR FOVs to the fixed MR FOV (and hence the PET FOV), harnessing the fact that MR gradients responsible for spatial encoding of images remain fixed throughout all studies. Using the described setup, PET/MR information was acquired in real-time to follow the functional and metabolic status of the *in vivo* tumor microenvironment. Moreover, we show that the setup allows one modality to guide studies with the other within a single imaging session.

3.2.3 Materials and Methods

3.2.3.1 MR-compatible PET Insert for Simultaneous PET/MR Studies

Studies were done using a MR-compatible PET insert. The insert consists of a concentric ring of 16 lutetium oxyorthosilicate (LSO) scintillators and position sensitive avalanche photodiodes (PSAPDs) detector modules. The intact system is designed to fit within the bore of a Bruker Biospin 7 T magnet fitted with a Bruker B-GA12 gradient coil set (12 cm ID, 40 G/cm maximum, 0.2 G cm A). The FOV offered by this PET setup is $35.35 \times 35.35 \times 12 \text{ mm}^3$. Previous reports demonstrated little to no interference between the PET and MRI electronics enabling PET and MRI images to be obtained at the same time [105]. PET data were acquired using in-house developed software [162], while the MR console was run by PARAVISION (Bruker Biospin Inc., Billerica, MA) software. Since the gain of the PSAPD detectors is temperature dependent, the detectors were kept at -12.5°C for all studies using a continuous flow of chilled dried air.

3.2.3.2 PET/MR Image Alignment

We explored whether alignment using an external phantom can give accurate registration over the course of a study day, as well as over multiple days. An “alignment” phantom consisting of rods filled with $\sim 50 \mu\text{Ci}$ ^{18}F -fluoro-deoxyglucose (FDG) solution was imaged simultaneously with both PET and MR. The rods used were glass capillary tubes (OD/ID = 1.2/0.68 mm) sealed at the ends with tube sealer (Becton Dickenson, Franklin Lakes, NJ). A model of the alignment phantom is shown in figure 3.9. For all PET studies, counts were acquired over 300 s and reconstructed with a maximum *a posteriori* algorithm [61] to a matrix size of $128 \times 128 \times 15$ and a pixel size of $0.276 \times 0.276 \times 0.754 \text{ mm}^3$. MRI images were obtained with a 2D spoiled gradient echo (FLASH) sequence (TR/TE = 350/4 ms) with a matrix size of 128×128 , and 40 contiguous slices resulting in a pixel size equivalent to that of the PET images. The FOV of the MR ($35.35 \times 35.35 \times 25.6 \text{ mm}^3$) is larger than the PET ($35.35 \times 35.35 \times 12.8 \text{ mm}^3$) to ensure that the whole PET FOV is captured by the MR FOV and hence allow proper alignment between the two image bases. This MR FOV is denoted hereafter as the home FOV, FOV_{home} . Setting the FOV_{home} as the reference basis, a semiautomatic alignment procedure was adopted to match the two spaces. First, the rod phantoms along the z direction (axial) were matched manually between the PET and MR images. As the spatial resolution of the PET along the axial direction as well as the outer diameter of the rods themselves dictate that one rod in the alignment phantom will traverse multiple PET slices, the central slice of the rod in both PET and MR was used to match the two bases along the z direction. The centroid of the rod cross sections perpendicular to the z direction served as inputs for alignment in the xy plane. Voxels within five voxels of the local maximum and with intensity above 20% of the local maximal intensity were considered in a center of mass calculation of each centroid. Points were fed into a least-squares 2D affine transformation algorithm implemented in MATLAB [163]. These two steps combine to derive a 3D affine transformation matrix. This matrix obtained at the beginning of the imaging session was stored and used for all subsequent image alignment. We measured the centroid registration error between the MR images and transformed PET images of the alignment phantom using the same transformation matrix over the course of a single day of imaging as well as over several days of imaging, with the centroid of the rod cross sections on multiple image slices as the metric. The alignment phantom was unloaded and loaded between these

scans to simulate a normal *in vivo* imaging session day.

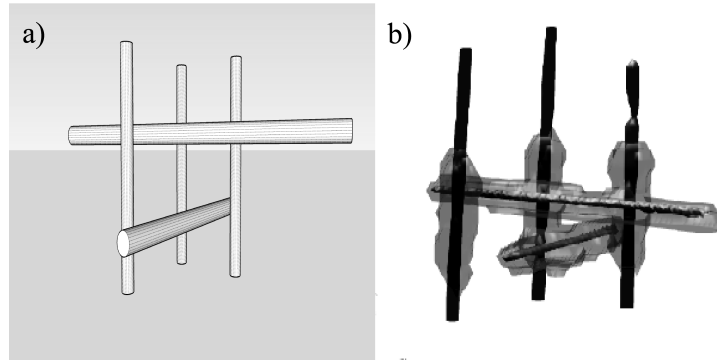


Figure 3.9: PET/MR FOV alignment phantom. (a) Rendering of PET/MR phantom. The phantom consisted of five rods, three in the z-direction for xy plane alignment and two parallel to the xy plane for z slice alignment. The latter are spaced 5 mm apart. The rods were filled with ^{18}F FDG solution. (b) PET/MR phantom image overlay. MR image rendering is given as narrow rendered objects (black); PET image rendering is wrapped around the MR rods (light grey).

To estimate the positioning accuracy of this alignment scheme as a function of location within the FOV, a phantom consisting of glass capillaries (OD/ID = 0.85/0.4 mm), filled with $\sim 50 \mu\text{Ci}$ FDG diluted in 0.05 M Prohance, and located 0, 4, 8, and 12 mm radially from the center of the FOV was imaged simultaneously with PET/MR and aligned using an independently determined transformation matrix derived as above, using the alignment phantom shown in figure 3.9. PET/MR images of this phantom are shown in figure 3.10. The centroid registration error as a function of distance from the center of the FOV was then evaluated as above. One-way ANOVA analysis was used to evaluate whether there were significant differences in registration between rods at different locations within the PET FOV. In section 3.2.7.1, we compare the alignment accuracy between images acquired with different MRI pulse sequences, with and without the PET insert, demonstrating good geometric matching between images taken with different sequences, also with and without the PET insert. In section 3.2.7.2, we compare the alignment accuracy between images registered with different transformations, showing that registration with the affine transformation is slightly better than using the rigid body transform.

The fidelity of this registration scheme was further tested with a third phantom and ^{18}F -FDG studies on mice containing small subcutaneous tumors (MC38.CEA colorectal adenocarcinoma). Experiments involving the use of animals were done in accordance with protocols approved by the Animal Care and Use Committee of the California Institute of Technology.

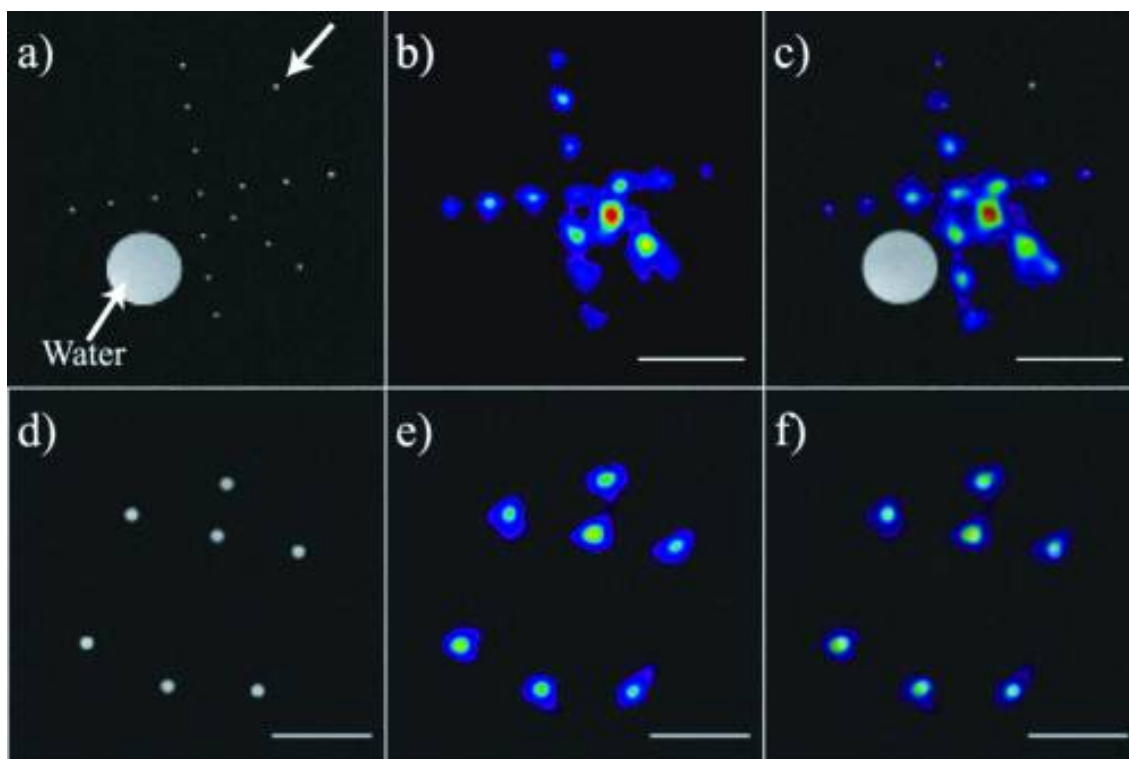


Figure 3.10: PET/MR FOV alignment strategy registers other phantom sets robustly. (a)–(c) Structured phantom used to evaluate alignment accuracy as a function of location within the FOV. Rods were located at 0, 4, 8, and 12 mm from the center of the PET/MR FOV. Alignment accuracy was evaluated after registration using a transformation derived from the alignment phantom. (a) MR image of the phantom. (b) PET image of the phantom. (c) Fused dataset. A large circular water phantom, shown as the large circle in (a) and (c), was inserted into the phantom to facilitate shim, frequency, and gain adjustments of the MR. One capillary rod was filled with water only and thus was visualized in the MR but not in PET (arrow). (d)–(f) The transform derived to form the overlay in figure 3.9 was used to fuse an image containing an alternative phantom arrangement. (f) Fused PET/MR image of a seven rod phantom shows the fidelity of the transform. (Scale bars=10 mm).

Alignment of Multiple MR FOVs

Often it is advantageous to optimize the orientation and size of the MRI FOV to accommodate a specific imaging goal. For simultaneous PET/MR imaging, care needs to be taken to ensure that the alternate MR FOV (FOV_{alt}) overlaps adequately with the PET FOV for the desired region of interest. For quick visualization of the PET and MR FOVs during an imaging session, we use the geometry defined by the MRI metadata to generate Cartesian coordinates of the centroids and vertices for each voxel of both the PET FOV and the alternate MR FOV. These values are used to visualize the “bounding box” of both FOVs in the same coordinate system, which allows a quick determination of the suitability of the FOV_{alt} for PET/MR imaging.

To generate aligned PET/MR datasets, the PET image registered to FOV_{home} , as described in section 3.2.3.2, is first resliced to an isotropic voxel size of $0.276 \times 0.276 \times 0.276 \text{ mm}^3$. It then undergoes a rigid body transformation using the transformation matrix from MRI metadata, and subsequently resliced to the voxel size of the alternate MR FOV. The whole data stream is implemented in MATLAB; a trilinear interpolation is used for all rotations and reslicing.

To demonstrate the feasibility of this method, we simulated the mapping on phantom images using different geometries that we typically encounter in our studies. An oblique slicing simulating an acquisition along an aortic vessel and a geometry that is offset and sampled at a different matrix size than the home FOV were aligned with simultaneously acquired PET data. This method was also used to remap a PET dataset to a mouse anatomical reference image.

3.2.3.3 Biological Studies with PET/MR: a Real-time Feedback Scheme

TgCEA⁺C57BL/6 mice (N = 2) were implanted with MC38.CEA colorectal adenocarcinoma cells in the groin and shoulder seven days prior to imaging. Mice were fasted 8-12 h prior to the imaging session to minimize extraneous ^{18}F -FDG signals. One hour prior to the imaging session, each mouse was injected intraperitoneally with $200 \mu\text{Ci } ^{18}\text{F}$ -FDG. The mouse was then placed in the PET/MRI system and kept at $\sim 37^\circ\text{C}$ with warm air blowing through the RF coil and anesthetized using 1.5% isoflurane mixed in air. The holder was designed in such a way that the mouse was kept comfortable while the PET insert remained stable at its operating temperature. Using the known alignment matrix, we shifted the expected region of functional interest, in this case the tumor, within

the PET FOV using the motorized stage. Once aligned, high-resolution anatomical MRI (2D RARE TR/TE = 3500/4.5 ms, matrix size = $128 \times 128 \times 34$, resolution = $0.276 \times 0.276 \times 0.754 \text{ mm}^3$) and PET (300 s duration) scans were obtained simultaneously. Both PET and MR images were respiratory gated to acquire data during the expiration phase.

Alignment time per PET dataset was 5–15 min (AMD, 4× Dual-Core Opteron 885 2.6 GHz, 32 GB memory). This relatively rapid calculation time allows processing and analysis of the PET/MR data while the animal is still in the scanner. Analysis of the processed PET/MR images of ^{18}F -FDG uptake within the MC38.CEA tumors was used to guide the next stage of the experiment. Heterogeneous PET signal within the tumor was verified using ^1H (MRS). We used the PET signal distribution to delineate ROIs for metabolic studies using ^1H MRS (PRESS with VAPOR water suppression, spectral width 8 kHz, 900 averages with 8192 sample points, TR/TE = 1685/10 ms, $3 \times 3 \times 3 \text{ mm}^3$, duration = 26 min). Three voxels were used for MRS imaging; one in the tumor at the region of high FDG uptake, one in the tumor at a region of low FDG uptake, and one in the contralateral muscle. The resultant spectra were processed and analyzed using Bruker TOPSPIN software (Bruker Biospin, Fremont, CA). A two-sided student's t-test was performed to compare the ratios between the high and low FDG regions.

3.2.4 Results

3.2.4.1 PET/MR Image Alignment

Figure 3.9 shows the overlay of PET and MR surface rendering of the alignment phantom images. Slices along the z-axis in figures 3.11 show the alignment along both the z direction and in the xy plane and demonstrate the difference in the resolution of the PET and MR images. Rods orthogonal to the z direction span multiple slices in the PET images. This is due to a combination of two factors. First, because the outer diameter of the rods is 1.2 mm and the mean positron range of the glass is $\sim 190 \mu\text{m}$, annihilation events from the ^{18}F -FDG can occur at the outer edge of the rod, which spans multiple image slices. Second, the spatial resolution of the PET along the axial direction is lower than the image slice thickness ($\sim 2 \text{ mm}$). Table 3.3 shows the mean and standard deviation of the centroid registration error in all three orthogonal directions for the alignment phantom images over the course of one and multiple days. In all directions, registration remained consistently at subvoxel

accuracy (maximum mean alignment error = 0.21 mm, voxel size = $0.276 \times 0.276 \times 0.754 \text{ mm}^3$) and well within the resolution limits of PET. This alignment procedure ably aligned alternate second rod phantom, as shown in figure 3.10 and table 3.3.

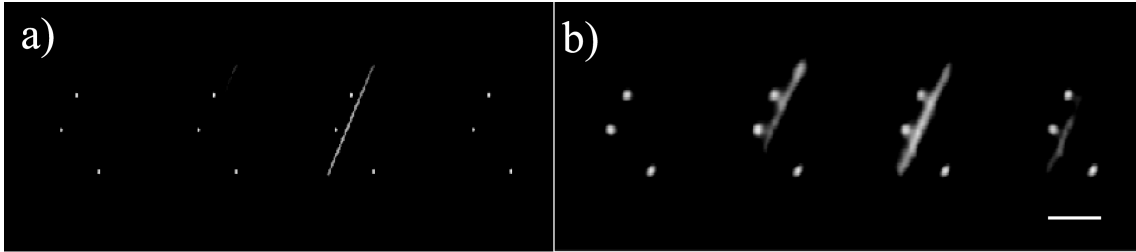


Figure 3.11: Different spatial resolution of the PET and MR images. (a) MR xy slices of aligned phantom. (b) PET slices corresponding to (a). Due to the lower spatial resolution of the PET along the axial direction and the positron range in glass matching the thickness of the capillary walls, the rod which was mostly displayed within one slice in the MR image spans almost three slices in the PET image. (Scale bar = 10 mm).

Table 3.4 shows the registration error as a function of location within the FOV. The alignment remained within <0.28 mm in accuracy throughout the whole FOV, with the mean centroid registration error ranging from about 0.18 mm in the center of the FOV to 0.28 mm at 12 mm from the center of the FOV. One-way ANOVA analysis show no significant difference between the mean registration errors at 0, 4, 8 and 12 mm from the center of the FOV in both the x ($p = 0.8$) and y ($p = 0.5$) directions.

We tested the alignment accuracy *in vivo* by imaging small xenograft tumors. Figure 3.12 shows aligned mouse PET/MR images at the level of the tumor and heart, with high ^{18}F -FDG uptake in both cases well within the expected anatomical regions.

3.2.4.2 Alignment of Multiple MR FOVs

Figure 3.13 shows the MR, PET and overlaid PET/MR datasets for common geometries used for PET/MR studies. In all cases, voxel grid alignment of the aligned PET images yielded good fit to the MR dataset.

Table 3.3: Centroid alignment error of phantoms using the PET/MR transformation scheme over multiple days. Units are in millimeters.

(mm)	PET/MR alignment phantom						Figure 3.2 (d) phantom	
	Day 1	Day 1	Day 2	Day 2	Day 3	Day 3	Mean offset	SD
X error	0.22	0.18	0.17	0.15	0.2	0.17	0.18	0.33
Y error	0.15	0.65	0.12	0.1	0.09	0.24	0.21	0.34
Z error	0.09	0.23	0.17	0.18	0.17	0.23	0.19	0.28

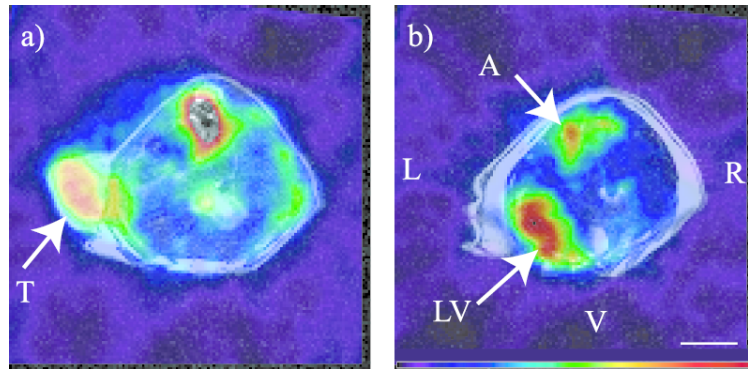


Figure 3.12: (a) PET/MR overlaid images at the level of a subcutaneous MC38.CEA flank tumor showing alignment of high ^{18}F -FDG uptake at the tumor site. (b) Image volume rostral to (a) showing corresponding high ^{18}F -FDG uptake at the left ventricle and aorta (T = tumor, LV = left ventricle, A = aorta, L = left, R = right, V = ventral, scale bar = 6 mm).

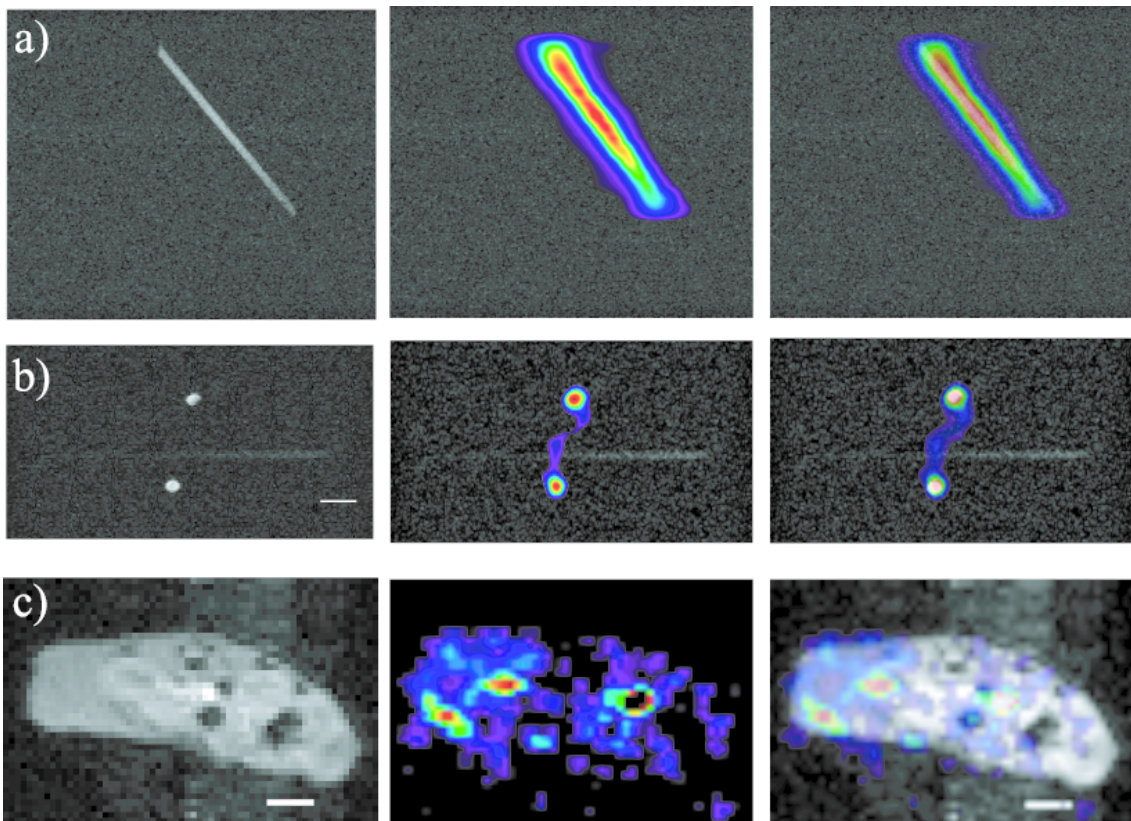


Figure 3.13: PET/MR alignment using different geometries. (a) MR slicing of a phantom along the coronal direction, at an oblique angle (40° on the left/anterior plane). (b) MR slicing along the axial direction, rotated 30° . The home coordinate system of the MR gradient set is noted to the left. (c) FDG-PET image of a mouse tumor obtained with axial slices at a FOV ($35 \times 28 \times 3 \text{ mm}^3$) smaller than FOV_{home} ($35.35 \times 35.35 \times 25.6 \text{ mm}^3$). Voxel grid alignment of PET image shows intratumoral heterogeneous uptake while accurately aligning high activity within the ureters (T = tumor, U = ureters, scale bars = 10 mm).

Table 3.4: Centroid alignment error as a function of location within the transaxial field of view, as measured by the phantom shown in figure 3.10. Units are in millimeters.

(mm)	Location from center of PET/MR FOV							
	0		4		8		12	
	mean	SD	mean	SD	mean	SD	mean	SD
X error	0.12	0.01	0.19	0.13	0.21	0.16	0.28	0.27
Y error	0.19	0.11	0.18	0.12	0.17	0.12	0.24	0.22

3.2.4.3 Real-time Feedback Studies with PET/MR Allows Multimodal Imaging of Biological Processes

Large tumors exhibit heterogeneous structures due to many factors [164]. Figure 3.14 shows that heterogeneous uptake of the glycolytic marker ^{18}F -FDG is seen within a thigh tumor. This heterogeneity was not readily apparent in the anatomical MR image. To explore this heterogeneity, MRS was obtained in ROIs guided by the variability of ^{18}F -FDG uptake shown in the PET images. ^1H MR spectra centered in regions of high ^{18}F -FDG uptake in the tumor showed a higher choline/creatinine ratio compared to ROIs in low ^{18}F -FDG areas and muscle (table 3.5).

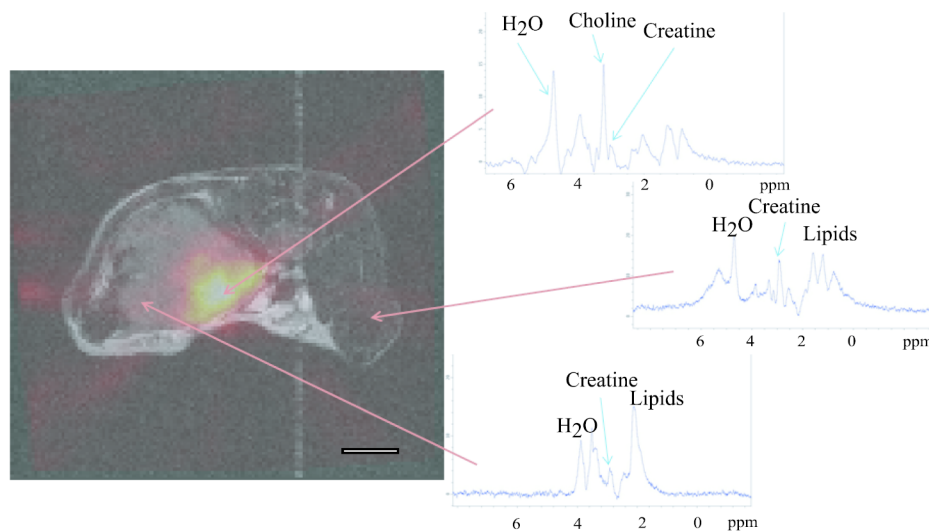


Figure 3.14: PET guided MRS assay of MC38.CEA tumor. Regions of differential ^{18}F -FDG uptake within the tumor were used to define the ROIs for ^1H MRS of the tumor. Spectra show differences between regions of high FDG uptake, low uptake, and contralateral muscle. (Scale bar = 3 mm).

Table 3.5: FDG-PET signal from xenograft tumors (N = 2) were used to guide ^1H MRS in different PET signal regions. Choline/creatine ratio were significantly different between high and low FDG regions ($p = 0.02$).

Region	Choline/creatine ratio
High FDG tumor region	3.4 ± 0.4
Low FDG tumor region	1.9 ± 0.3
Muscle	Negligible

3.2.5 Discussion

In this study, we demonstrate the feasibility of performing robust *in vivo* studies with simultaneous PET/MR imaging using a PET insert placed in a small animal MR scanner. Given the spatial constraints within the PET insert and animal holder, a method in lieu of the traditional fiducial marker system is required to ensure robust registration of the two modalities. Once the PET insert is fixed within the MR scanner, the relative orientation of the PET (as determined by the placement of the LSO crystal detectors) and MR (as determined by the placement of the imaging gradient set) coordinate systems is also fixed. Thus the transformation matrix that registers images using a single alignment phantom also brings together all subsequent PET/MR images. We confirm this by repeatedly registering the PET and MR images of the alignment phantom over a study session and over multiple days with subvoxel accuracy (table 3.3) using one transform matrix. This alignment is not dependent on the location within the FOV (table 3.4). Images of an alternate phantom and tumor bearing mice also support this alignment accuracy (figure 3.12). Straightforward registration of the PET and MR image spaces using a predetermined transformation matrix allows for an uncomplicated multimodal imaging scheme, whereby neither a specially designed PET/MR holder nor an animal mold [112, 165] is required for image alignment. This setup provides imaging flexibility; first, there are no potential intensity spillover effects due to an external radioactive marker, which may make low activity ROIs or ROIs close to the marker difficult to discern. Second, this method of alignment allows alternate MRI transmit/receive coil setups to be used without the need for a new alignment scheme, since the registration is based on the spatial encoding provided solely by MR gradient coils. This will be useful for studies that use a surface coil to achieve high SNR. Ideally, the alignment method used should be fully automatic, although previous reports have indicated that partial manual manipulation of images during processing may yield sufficient alignment

accuracy [166]. We adopt a manual alignment of the z direction because of the disparate FOV sizes between the PET and MR along that axis. As we make no prior assumption about the physical FOV alignment along this axis, a large MR FOV is taken to ensure full coverage of the PET FOV. From our observations, the removal and replacement of the PET insert within the MR scanner can cause up to 1.5 slices (~1 mm) displacement between the PET FOV and that of the MRI. Studies are in progress to design a phantom alignment setup along the lines of previous designs for PET/CT systems [153, 151, 152] that will allow fully automated alignment. Nevertheless, the general alignment strategy will remain the same as described here regardless of the phantom setup used.

One notable difference between MR and CT acquisition is the need to alter the imaging geometry in MR to maximize the SNR and to obtain images at the desirable orientation or resolution. This is especially relevant for *in vivo* applications; a compromise must be struck between a realistic scan duration time and the resolution of the acquired image. In MR-only studies, the FOV can only be determined once the animal is loaded inside the scanner. The limited PET FOV adds an extra geometry constraint for PET/MR studies. We have developed a simple software GUI visualizing the overlay of the PET and MR FOVs to allow a quick check to ensure that our anatomical regions of interest lie completely in the useful PET FOV prior to image acquisition.

The constrained geometry of the PET/MR system (which limits the use of external fiducial markers) and the imaging flexibility of the MR require a robust method to coregister PET and MR images with multiple FOV geometries. In previous studies, this has been addressed by making assumptions about the anatomical distribution of the functional PET signal [167, 168, 169] using a transmission source or implanting fiducial markers [165]. The first two strategies may not yield an optimal solution if the distribution of the PET signal is unknown or heterogeneous, while the latter is invasive. Given the fact that the PET is fixed physically within the MR during a single imaging session, a simple algorithm was developed that aligns the voxel grids of the “home” PET/MR FOV to any alternate MR FOVs. We make the assumption here that the MR gradients behave consistently between different scans such that the images acquired at a set geometry in software is the same in the hardware. Common Fourier imaging, as described by the k-space formalism [170], relies on spatial encoding determined by spatially and temporally varying magnetic fields created by the MR gradients. Advances in hardware design of gradient coils [171] and post-acquisition

processing [172, 173, 174] means that most commercial scanners have robust gradient performance, especially for the pulse sequences using Cartesian k-space trajectories (see [64, 175] for discussion of gradient coil design, specifications, and performance). From a simultaneous PET/MR viewpoint, the pertinent concern is that the presence of the PET insert inside the gradient set may distort the generated gradient fields. Previous characterization of APD-based PET inserts has demonstrated that MR images acquired in the presence of the PET insert show negligible geometric distortions compared to those acquired without the PET [105, 102] (see also section 3.2.7.1).

In our implementation, we transform the PET image to match that of the MR images. We chose this approach because the resolution of the PET is lower than the MR, so there would be less potential loss of information from image interpolation. Also, the PET FOV is fixed and typically smaller than the MR FOV, so this approach also simplifies the formation of the fused dataset. Other interpolation methods, apart from trilinear interpolation, can be adapted to improve the quantitative value of the transformed images [176, 177]. However, the interpolation method we adopted should suffice for PET images. Simulation of some common geometries that require this schema show that the registered PET images align well with the corresponding MR image (figure 3.13). The algorithm described is time efficient; all datasets generated took 20 min or less.

Simultaneous PET/MR imaging allows examination of the different signals in both spatial and temporal registration. In figure 3.14, we see heterogeneity within a tumor microenvironment highlighted with both ^{18}F -FDG-PET imaging and high-resolution anatomical MRI. ^1H MRS, guided by the ^{18}F -FDG signal, confirms the heterogeneous profile of the tumor. Rapid reconstruction, processing, and visualization of the aligned initial PET/MR images provide the information necessary to perform the later MRS study within the same imaging session. Thus, obtaining feedback between the two modalities during a single imaging session is eminently doable with this system. This will have multiple uses. Phantom alignment information allows us to position the mouse to maximize PET signal in the FOV. While new versions of the PET insert will aim to have whole body coverage, this is typically not feasible in clinical systems or in situations where one may want to sacrifice coverage for higher sensitivity and resolution. The feedback schema can also be performed during the experiment to guide study directions. The ability to process and align the PET/MR images quickly within an imaging session allows basic analysis of the combined dataset. In our study, this

allowed us to determine regions of tumor functional heterogeneity via ^{18}F -FDG accumulations and subsequently, ^1H MRS studies, to assess corresponding heterogeneity in metabolite concentration. Again, the external means of image registration proved useful in this situation; no assumption of the expected distribution of the image intensities in either image was used for alignment, allowing us to delineate the heterogeneity within the tumor. Although there is a correlation between the regions of high ^{18}F -FDG uptake and high choline/creatine ratio (table 3.5), more studies are required to determine the significance of this observation as the relationships between phospholipid metabolism and glycolysis remain unclear [178, 179, 54, 180, 181]. Further studies along these lines will involve correlating the tumor characteristics such as perfusion [182] and hypoxia [183] with these functional markers.

Simultaneous PET/MR technology has the potential to impact both preclinical and clinical realms. The time savings that can be obtained by doing two scans at once will facilitate the efficiency of longitudinal studies. Cross-modal image corrections methods such as MR-guided PET motion and attenuation correction, which rely on robust PET/MR coregistration, will improve image quality and aid image interpretation [89, 88]. Perhaps more importantly, like the development of multicolor fluorescent proteins and dyes that allow multiple processes to be studied concurrently [184, 12], simultaneous PET/MR will enable similar interactive studies to be done within intact mammalian systems. Molecular imaging agents are being developed with both PET and MR contrast that can look at biological processes such as gene expression [58], receptor binding [120, 57], cell tracking [185], and vascular inflammation [186]. Combining these agents within one study will allow multiple physiological processes to be probed simultaneously.

3.2.6 Conclusions

We describe a coregistration design for performing time-sensitive *in vivo* studies using a simultaneous PET/MR scanner. Robust image registration between PET and MR is shown, based on the fixed relative orientation of the PET detectors and MR imaging gradient set. Using this setup, we demonstrate heterogeneous metabolic activity within a tumor using ^{18}F -FDG-PET, which was found to correlate with choline/creatine ratios determined using MRS guided by the ^{18}F -FDG signal levels.

3.2.7 Supplemental Data

3.2.7.1 Comparison of Alignment Accuracy Between Images Acquired with Different MRI Pulse Sequences

Methods. A hot rod phantom filled with water was imaged with three different MR pulse sequences at the same FOV and matrix size ($35.35 \times 35.35 \times 0.754 \text{ mm}^3$ and $128 \times 128 \times 1$ respectively):

1. A 2D spoiled gradient echo FLASH sequence (TR/TE = 500/4.4 ms)
2. A 2D spin echo RARE sequence (TR/TE = 2000/11 ms)
3. A 2D EPI sequence (TR/TE = 1000/20.4 ms), acquired in 4 shots. The Bruker native gradient adjustment macro *EPI_ADJUST*, which compensates for the time lags of the gradients and filters and the first order eddy currents, as executed prior to image acquisition. No other correction was applied.

The acquired images were then coregistered to determine the registration error between them. A rigid body registration algorithm was used [163]. We calculated the translational and rotational mismatches from the resultant transformation matrices.

This was repeated with and without the PET insert being powered on. Five images were acquired for all pulse sequences for both conditions. Registration differences were compared for all images in a combinatorial manner.

Results. Figure 3.15 shows sample images acquired with the three sequences. Both translation and rotation differences between images acquired by the three pulse sequences are shown in table 3.6. Alignment between the RARE and FLASH images show lower translational and rotational registration difference compared to EPI. This is expected, as the EPI sequence is inherently more prone to geometric distortions compared to the other two pulse sequences. A two-way ANOVA examining the translational differences of the three different image comparisons with and without the PET powered on showed no significance differences between the comparison groups ($p = 0.06$) and whether the PET is on or off ($p = 0.69$). In contrast, analysis of the rotational differences showed a significant difference between groups ($p = 0.01$), PET power status ($p < 0.01$) and their interaction

($p = 0.05$). Although this is the case, it must be noted that the absolute values of the rotational differences are $<0.01^\circ$. Coupled with the <0.2 mm translational offset for all the comparison groups, this alignment difference remains well within the spatial resolution of PET and supports the claim that our methodology is robust enough to coregister PET/MR images accurately. Of course, this is under the proviso that the MR images are properly corrected, as one would do for any MR-only experiment.

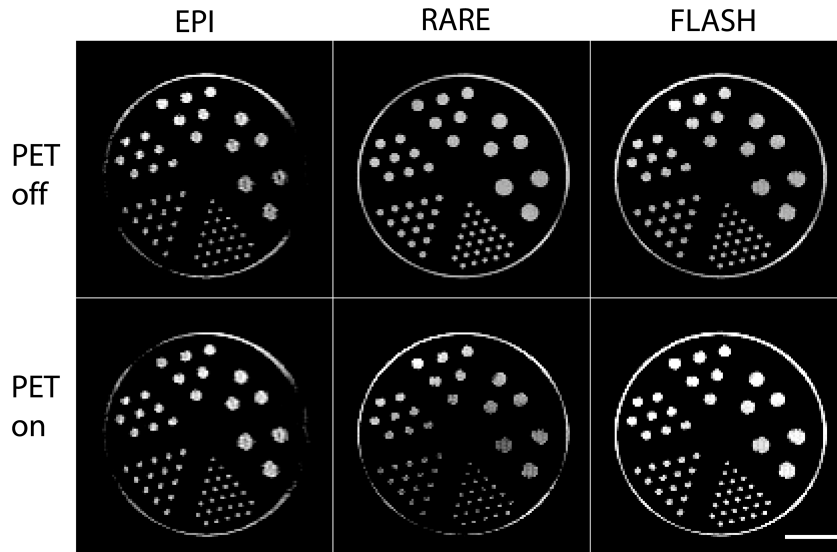


Figure 3.15: Images acquired with different pulse sequences and with PET on and off show no noticeable geometric distortions, enabling robust PET/MR coregistration; see table 3.6 (Scale bar = 10 mm).

Table 3.6: Alignment displacements between images acquired by different pulse sequences. Images were aligned by a 2D rigid body algorithm; the translational and rotational terms were used to determine the displacement and rotational offset between images.

Sequence A	Sequence B	PET powered status	Translation offset (mm)		Rotation offset (degrees)	
			mean	SD	mean	SD
EPI	RARE	On	0.05	0.09	0.001	0.01
EPI	RARE	Off	0.04	0.05	0.009	0.01
EPI	FLASH	On	0.07	0.1	0.002	0.01
EPI	FLASH	Off	0.07	0.11	0.008	0.01
RARE	FLASH	On	0.03	0.03	0.001	0.001
RARE	FLASH	Off	0.06	0.01	0.001	0.001

3.2.7.2 Comparison of Alignment Accuracy Between Images Registered with Different Transformations

Methods. The same dataset used in section 3.2.3.2 was coregistered by two additional methods:

1. Same as section 3.2.3.2, except a rigid body transformation algorithm was used.
2. A 3D rigid body algorithm, as implemented in 3D-Slicer version 3.4 (www.slicer.org), was used.

For method 2 above to work, PET images had to be pre-processed manually to approximately align the PET and MR space before being fed into the 3D algorithm. Without the pre-processing step, the algorithm tends to over-rotate the PET image, pushing one of the rod sources out of the FOV

Results. Table 3.7 and table 3.8 show the registration alignment error by both the 2D and 3D rigid body algorithm respectively. Both algorithms yielded good registration, which was not significantly different from the affine ($p = 0.76$). The affine transformation was slightly better than the rigid body algorithms (the Euclidean distance of the mean alignment errors for the affine, 2D rigid body and 3D rigid body transformations were 0.34, 0.38, 0.36 mm respectively). It must also be noted that a manual preprocessing step is required to approximately align the PET/MR dataset for the 3D algorithm to work.

Table 3.7: Centroid alignment error of phantoms using the PET/MR transformation scheme over multiple days, using a 2D rigid body transformation. Two-way ANOVA analysis comparing between x, y, z errors showed no significant differences between groups ($p = 0.66$), nor between rigid and affine transformations ($p = 0.51$). Both rigid and affine transforms yielded alignment errors well within the PET spatial resolution.

PET/MR positioning phantom									
(mm)	Day 1	Day 1	Day 2	Day 2	Day 2	Day 3	Day 3	mean	SD
X error	0.2	0.2	0.22	0.18	0.2	0.27	0.22	0.21	0.03
Y error	0.16	0.74	0.17	0.18	0.2	0.18	0.15	0.25	0.22
Z error	0.09	0.23	0.18	0.25	0.29	0.14	0.16	0.19	0.07

Table 3.8: Centroid alignment error of phantoms using the PET/MR transformation scheme over multiple days, using a 3D rigid body transformation. Two-way ANOVA analysis comparing between x, y, z errors showed no significant differences between groups ($p = 0.64$), nor between rigid, affine and 3D rigid transformations ($p = 0.76$). All transforms yielded alignment errors well within the PET spatial resolution.

PET/MR positioning phantom									
(mm)	Day 1	Day 1	Day 2	Day 2	Day 2	Day 3	Day 3	mean	SD
X error	0.25	0.2	0.19	0.38	0.21	0.24	0.3	0.25	0.07
Y error	0.2	0.19	0.25	0.19	0.17	0.14	0.25	0.2	0.04
Z error	0.13	0.03	0.43	0.51	0.46	0.05	0.32	0.17	0.2

3.3 Phantom Designs for Robust *In Vivo* Coregistration of Hybrid Imaging Systems: Comparison of Semiautomatic and Automatic Approaches

3.3.1 Introduction

Increasing efforts are being devoted to develop and validate hybrid techniques for multimodality imaging of biological processes *in vivo*. Several dual modality platforms have been successfully developed and tested. For example, positron emission tomography (PET) has been combined with computed tomography (CT), magnetic resonance imaging (MRI) [105] and optical tomography [187]. The major advantage of these methods lies in the possibility of imaging the same living subject in a single session, in some cases simultaneously. A vital component for multimodal imaging is the requirement of accurate spatial coregistration of the separate image spaces. Significant efforts have been devoted to cross-modal registration in small animal imaging, based upon optimizing animal holders and utilizing manually segmented phantom designs. Hybrid imaging systems adds an extra complexity; the geometry constraints of integrated systems along with the disparate field of view between the individual modalities require a modification to previous approaches. A registration phantom design that can be adapted for different hybrid systems and can perform image registration automatically is highly desirable.

Here, we evaluate a phantom design adapted for use in a MR-compatible PET insert for simultaneous PET/MRI imaging. The phantom design allows simple image acquisition, fully automatic segmentation of the phantom components and subsequent image coregistration. We compare the registration error of this fully automated strategy with our previous semiautomatic alignment strategy outlined in section 3.2. Both strategies aligned the PET and MR image spaces to within single voxel accuracy throughout the whole field of view of the combined scanner with no significant difference of registration errors (two-sample t-test: $p = 0.2$). In addition to providing equivalent coregistration results the automatic alignment strategy guarantees a non-biased, fast and versatile tool which could be adapted easily for other types of combined imaging systems.

3.3.2 Materials and Methods

3.3.2.1 Semiautomatic Alignment Phantom

The semiautomatic alignment phantom was constructed as described in section 3.2.3.2.

3.3.2.2 Fully Automatic Alignment Phantom

The fully automatic alignment phantom consists of rods placed within a truncated 50 mL Falcon tube (BD). A Falcon tube was truncated to a length of 60 mm. Holes were drilled in the end caps (the native lid of the tube or a thick plastic cylinder) according to the pattern outlined in the schematic shown in figure 3.16. Holes were drilled to fit glass capillary rods (OD/ID = 0.7/0.5 mm, Wales Apparatus) snugly. The central rod was fitted diagonally across the diameter of the tube. Rods were filled with ~50 mCi of ^{18}F -FDG prior to placement in the tube. A tube filled with water (ID = 6.5 mm, Micronic) was placed along the inner edge of the tube in line with the central rod to facilitate MRI imaging.

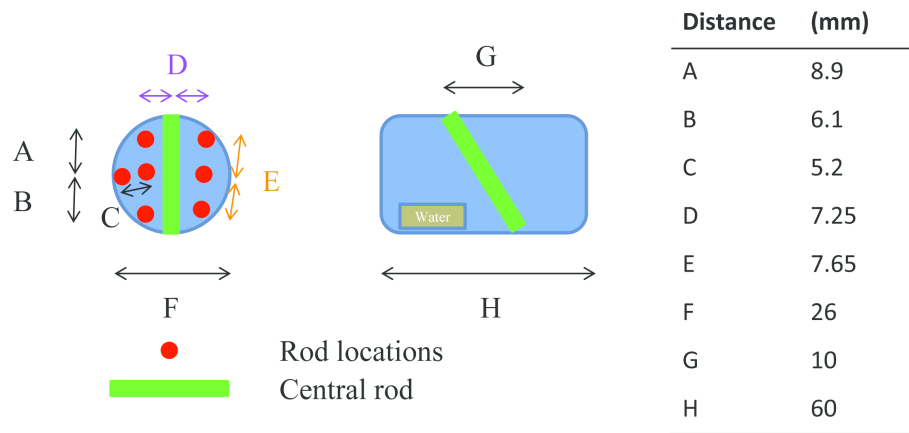


Figure 3.16: Schematic of automatic phantom. End cap view (left) and side view (right) of the phantom, with associated distance measurements are shown. The current phantom is implemented with a 50 mL Falcon tube. The asymmetric distributions of rods on either side of the central rod facilitates their segmentation. The presence of the water tube facilitates MRI.

3D renderings of both the semiautomatic and automatic alignment phantoms from PET/MRI datasets are shown in figure 3.17.

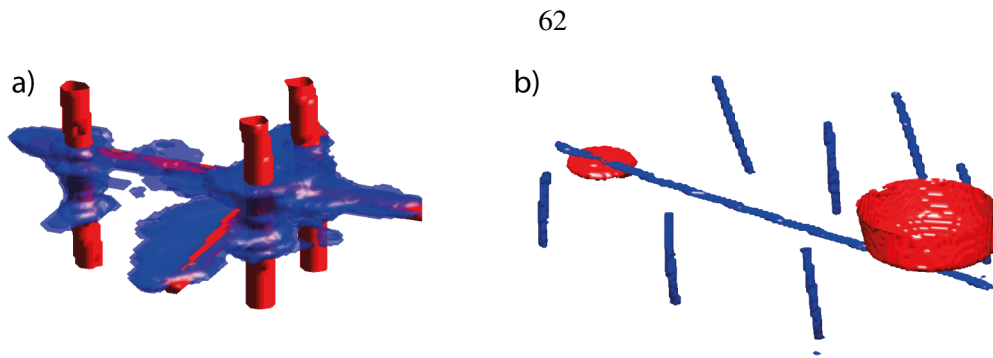


Figure 3.17: Semiautomatic (a) and automatic (b) alignment phantom models. Red denotes MR-visible portion of the phantom. Blue denotes PET/MR visible portion of the phantom. Glass capillary tubes filled with ^{18}F -FDG and saline enable multimodal visualization. In (b), large red portions are present to allow robust MRI shimming and adjustments.

3.3.2.3 Simultaneous PET/MRI Imaging

Phantoms were imaged using the MR-compatible PET insert combined with a 7 T Biospec small animal MRI. PET images were acquired with durations ranging between 300 and 600 s and reconstructed as described in section 3.2.3.2. MRI were obtained using a gradient echo FLASH (TR/TE = 350/4 ms, FOV = $35.35 \times 35.35 \text{ mm}^2$, slice thickness = 0.754 mm, 34 slices).

3.3.2.4 Semiautomated Alignment Strategy

PET and MRI datasets of the semiautomatic alignment phantom were aligned as described in section 3.2.3.2.

3.3.2.5 Fully Automated Alignment Strategy

PET and MRI datasets of the fully automatic alignment phantom were aligned using the following steps:

1. Each individual rod in the alignment phantom seen in both the MRI and PET images was segmented using an intensity-based algorithm. A predefined threshold of 25% of the maximum intensity of the image and a radius of $\sim 4 \text{ mm}$ was used to segment voxels belonging to each rod. The central rod was identified by the fact that it showed the greatest x/y displacement across the image slices. The other rods were identified using the fact that they were situated in a known orientation about the central rod. The result of a sample segmentation is shown in figure 3.18.

2. The axial FOVs of the MRI and PET datasets are different (25.6 and 12.8 mm respectively). We first aligned MRI and PET images along the axial directions using a procedure outlined in [151]. Briefly, the ratio of the distances between the central rod and two other rods in the phantom, as shown in figure 3.18, are calculated across all the imaging slices. These values were plotted as a function of slice number. A quadratic curve was fitted to the plots to reduce the effect of image noise or segmentation errors. At equivalent locations in the phantom, these ratios should be similar. Thus, the displacement between the minima of the PET and MRI plots corresponds to the axial displacement between the two datasets. Sample plots outlining this process is shown in figure 3.19.
3. Once axially aligned, the PET and MRI phantoms were aligned using a 3D affine transformation [188]. Rod coordinates from every slice were treated as individual points as an input to this algorithm. All alignment software was implemented in MATLAB.

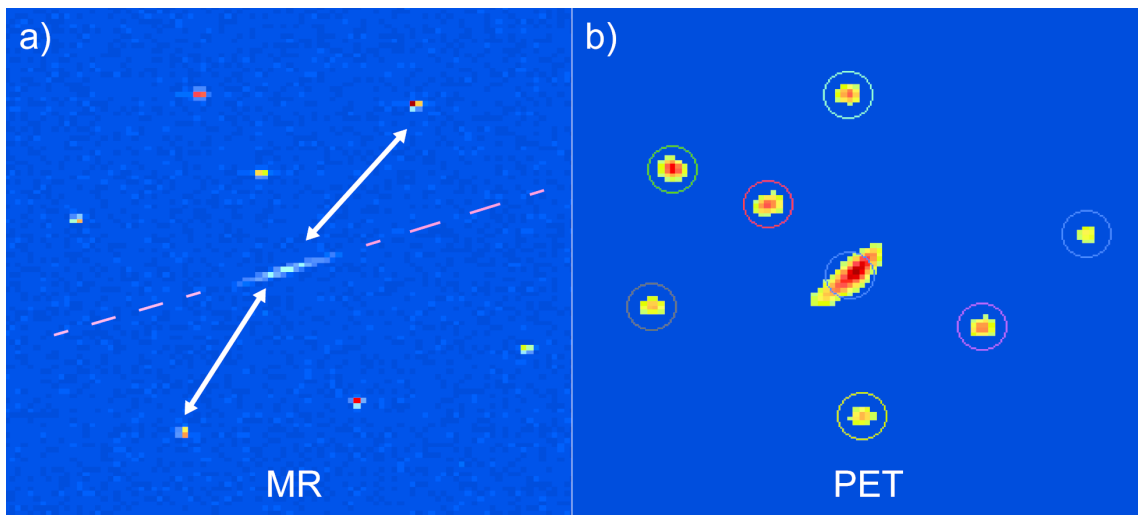


Figure 3.18: Automatic phantom rod delineation. a) MR image of phantom. Pink dashed line shows trajectory of central rod. White arrows show the two distances from which a ratio is derived. This changes according to axial position. b) PET image of phantom with circles showing automatic rod segmentation.

3.3.2.6 Evaluation of Alignment Accuracy

A separate PET/MRI image scan (acquired with the same parameters described in section 3.3.2.3) of the automatic phantom was used to evaluate the alignment accuracy of both methods. PET and MRI

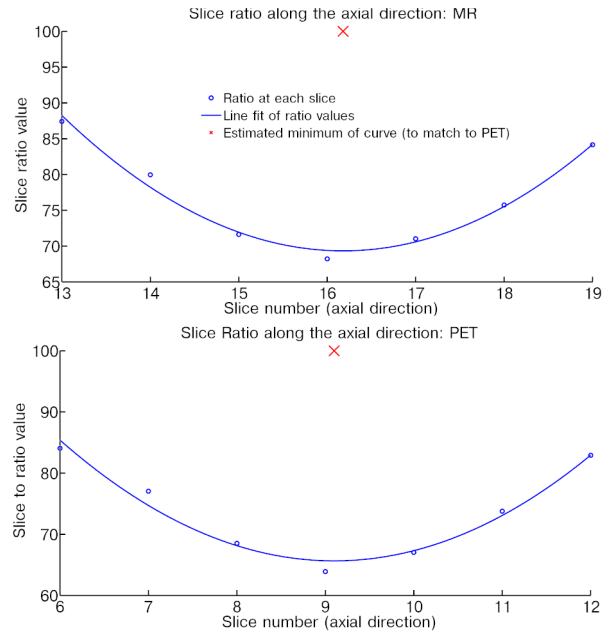


Figure 3.19: Automatic axial alignment of images. Due to the disparate field of views between modalities, we first approximately align in the axial direction. Ratios between a central, moving, rod and other rods were used to landmark slice positions. A quadratic fit reduced noise errors. The red X marks the minima of the PET and MR curves for axial matching.

images from this dataset were aligned with transformations derived from either the semiautomatic or automatic phantom alignment. The centroid alignment error of individual rods within aligned images were then calculated as per section 3.2.3.2.

3.3.3 Results

PET/MRI images of the semiautomatic and automatic phantoms are shown in figure 3.20. Figure 3.20 e shows an overlay of an automatic phantom image using a automatic alignment transform.

The centroid alignment error over x/y/z directions are shown in table 3.9. Both strategies aligned PET and MRI images within the image resolution of both systems (<0.3 mm). Although the mis-registration error for the semiautomatic alignment approach was slightly higher than the automatic approach, this was not significant ($p = 0.2$).

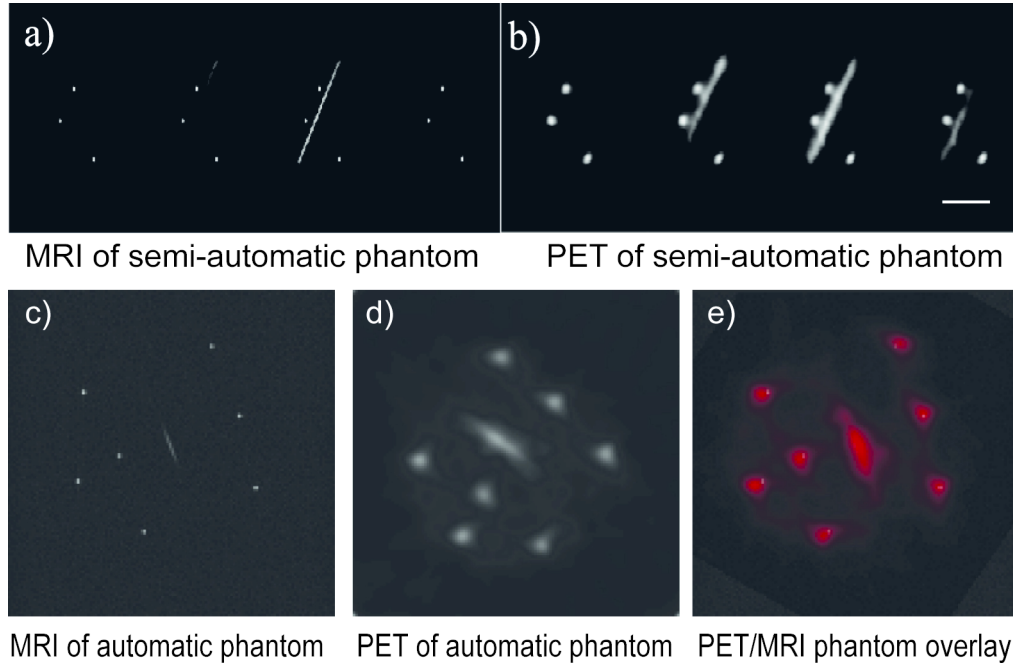


Figure 3.20: PET/MRI images of semiautomatic (a)-(b) and automatic (c)-(e) phantoms. Note in (b), the axial rods traverse multiple slices, which may lead to alignment errors. The configuration in (c)-(e) may reduce alignment errors and simplify registration. (Scale bar = 10 mm).

Table 3.9: Alignment error comparison between automatic and semiautomatic alignment methods.

Method	Alignment error (mm)	
	mean	SD
Semiautomatic alignment	0.26	0.16
Fully automatic alignment	0.11	0.1

3.3.4 Discussion

In this study, we developed a phantom that enabled automatic alignment of PET and MRI image spaces. Prudent design of rod locations within the phantom allowed facile automatic rod segmentation in both PET and MRI image sets. The presence of a sloping rod across the axial direction enabled automatic identification of axial location and subsequent alignment. This was necessary in our case because the FOVs of the PET and MRI were quite different, such that direct application of standard 3D alignment transform found in common image processing programs did not work.

Once the phantoms were axially aligned, we applied a closed-form algorithm for full 3D-

alignment. We chose this method over more common alignment algorithms again because of the different FOV sizes. Commonly found 3D alignment transforms [189] are iterative in nature. In phantom images with sparse signal, such as those encountered here, these algorithms can often result in a failure to converge to a reasonable solution. A closed-form solution based on matching points returns an exact result that can be easily implemented into an automatic pipeline.

Both semiautomatic and automatic alignment strategies were able to align the PET and MRI image spaces well within the spatial resolution limits of PET (~1–2 mm, whereas the alignment error was <0.3 mm) and were not significantly different. The automatic strategy returned slightly lower errors overall. This may be due to the fact that the automatic phantom contained more rods covering a larger portion of the FOV, thus improving the accuracy of the overall FOV alignment. Accuracy of the FOV alignment can be further improved by increasing the number of rods in the FOV, at the expense of increased computing time to segment the rods.

On a day-to-day basis, the semiautomatic phantom is an easier phantom to make and use since it requires fewer rods (5) than the automatic phantom (8). However, incorporation of a long half-life agent (such as ^{68}Ge) in the rods would enable a more permanent implementation of the automatic phantom. In this scenario, the automatic alignment phantom would be a simple and accurate method to ensure robust coregistration of the PET and MRI image spaces. Such a phantom is being explored for use in the second generation PET/MRI system.

In summary, we have developed a phantom that can align multimodal image spaces automatically. The phantom is straightforward to make and can fit in the tight geometries found in novel hybrid imaging systems. Alignment accuracy with this phantom was comparable with a previously developed semiautomatic approach. These phantom designs, when coupled with appropriate contrast agents (e.g. PET/MRI/CT/SPECT/optical dyes), can be used to align images acquired from multiple modalities with high accuracy.

3.4 Quantitative, Simultaneous PET/MRI for Intratumoral Imaging with a MR-compatible PET Scanner

3.4.1 Abstract

Noninvasive methods are needed to explore the heterogeneous tumor microenvironment and its modulation by therapy. Hybrid PET/MRI systems are being developed for small animal and clinical use. The advantage of these integrated systems depends on their ability to provide MR images that are spatially coincident with simultaneously acquired PET images, allowing combined functional MRI and PET studies of intratissue heterogeneity. Although much effort has been devoted to developing this new technology, the issue of quantitative and spatial fidelity of PET images from hybrid PET/MRI systems to the tissues imaged has received little attention. Here, we evaluated the ability of a first-generation, small animal MR-compatible PET scanner to accurately depict heterogeneous patterns of radiotracer uptake in tumors.

3.4.1.1 Methods

Quantitative imaging characteristics of the MR-compatible PET (“PET/MRI”) scanner were evaluated with phantoms using calibration coefficients derived from a mouse-sized linearity phantom. PET imaging performance was compared to a commercial small animal PET system (microPET R4) and autoradiography in tumor-bearing mice. Pixel and structure-based similarity metrics were used to evaluate image concordance among modalities. Feasibility of simultaneous PET/MRI functional imaging of tumors was explored by following ^{64}Cu -labeled antibody uptake in relation to diffusion MRI using cooccurrence matrix analysis.

This section is published in the *Journal of Nuclear Medicine*: Thomas S.C. Ng, James R. Bading, Ryan Park, Hargun Sohi, Daniel Procissi, David Colcher, Peter S. Conti, Simon R. Cherry, Andrew. A. Raubitschek, Russell E. Jacobs (2012) Quantitative, simultaneous PET/MRI for intratumoral imaging with a MR-compatible PET scanner. *Journal of Nuclear Medicine*, 53 (7).

Acknowledgments: We thank Dr. Kofi Poku for preparing the ^{64}Cu -DOTA-NHS-M5A antibody and Dr. Andrey Demyanenko, Desiree Crow, Alex Poznak, Sonia Collazo and Bitu Alaghebandan for their technical assistance. Drs. Yibao Wu and Scott Fraser gave helpful advice. The project was funded by NIBIB R01 EB000993, NCCR S10 RR015703, S10 RR019253, Beckman Institute, USC Molecular Imaging Center and the Caltech/City of Hope Biomedical Initiative.

3.4.1.2 Results

The PET/MRI scanner showed stable and linear response. Activity concentration recovery values (measured/true activity concentration) calculated for 4 mm diameter rods within linearity and uniform activity rod phantoms were near unity ((0.97 ± 0.06) and (1.03 ± 0.03) respectively). Intratumoral uptake patterns for both ^{18}F -FDG and a ^{64}Cu -antibody acquired using the PET/MRI scanner and microPET were highly correlated with autoradiography ($r > 0.99$) and with each other ($r = 0.97\pm 0.01$). Based on this, we performed a preliminary study comparing diffusion MRI and radiolabeled antibody uptake patterns over time and visualized movement of antibodies from the vascular space into the tumor mass.

3.4.1.3 Conclusions

The MR-compatible PET scanner provided tumor images that were quantitatively accurate and spatially concordant with autoradiography and the microPET R4. Cooccurrence matrix approaches enabled effective analysis of multimodal image sets. These observations confirm the ability of the current simultaneous PET/MRI system to provide accurate observations of intratumoral function and serve as a benchmark for future evaluations of hybrid instrumentation.

3.4.2 Introduction

The tumor microenvironment greatly impacts the efficacy of cancer treatment [1]. Factors such as heterogeneous perfusion and subpopulations of cells within tumors affect tumor progression and response to therapy. Investigations of these factors usually involve measurements at a whole tumor level (e.g. size) and tissue sampling for histological or biochemical assays. noninvasive imaging complements these studies by providing intact tissue information at multiple timepoints in the same individual [12].

The utility of multimodal imaging is well demonstrated in cancer research [14]. Advances in hybrid positron emission tomography/magnetic resonance imaging (PET/MRI) systems [190] show particular promise for understanding the heterogeneous nature of the tumor microenvironment. When spatially and temporally matched, high-resolution anatomical and functional information such as the perfusion status [191], cellular density [192] and metabolic status of specific tissue

regions acquired with MRI can enhance the interpretation of functional data provided by PET (e.g., oxygenation [183], cellular proliferation [53] and receptor expression [193]) and vice versa.

Conventional PET image analysis focuses on regions of interest (ROIs) encompassing whole tumors, with some studies omitting obvious “necrotic” regions during analysis [192]. Efforts to improve the spatial resolution of reconstructed PET images [194] and availability of coregistered PET and MRI have engendered interest in understanding the heterogeneity of radionuclide uptake observed with PET. For example, a recent clinical study by Metz, *et al.*, examined heterogeneity of tumor perfusion using MRI and correlated it with PET studies of integrin expression and tumor metabolism [195]. Similarly, Cho, *et al.*, compared MRI measures of tumor perfusion with uptake of the PET hypoxia tracer ^{18}F -MISO within rat tumor xenografts [183].

Correct interpretation of PET images, especially within regions of heterogeneous tracer uptake, requires that fidelity be verified between these images and actual tissue activity concentration patterns. Characterization of PET instrumentation usually entails measuring a standard set of metrics in a variety of phantoms [196], followed by gross *in vivo* verification. While this approach examines the general performance of the scanner, simple geometric patterns of phantoms may be insufficient to predict *in vivo* performance. To validate the heterogeneous spatial patterns seen in PET images, one needs to compare these images with a “gold standard” such as (QAR) [197].

We have evaluated the image quality of a first-generation, MR-compatible PET scanner (“PET/MRI scanner”) [160]. Previous reports used standard metrics to assess the performance characteristics of the scanner [198] and its ability to function within the integrated PET/MRI environment [105]. Here, we examined the image fidelity of the PET/MRI scanner and its ability to quantify heterogeneous uptake patterns in mice compared with QAR and a commercial small animal PET system. Phantoms were used to evaluate the quantitative capability of the PET/MRI scanner. Next, the three systems were used to image patterns of ^{18}F -fluoro-deoxyglucose and ^{64}Cu -antibody uptake within mice tumor xenografts. Finally, a preliminary, simultaneous *in vivo* diffusion MRI/radiolabeled antibody PET study was performed and a cooccurrence matrix method was applied to analyze the bimodal dataset.

3.4.3 Materials and Methods

3.4.3.1 MR-compatible PET Scanner

The PET/MRI scanner being evaluated has been described in detail [160]. The system fits in a Bruker–Biospin 7 T MRI system run using PARAVISION4 (Bruker-Biospin). PET data were acquired using custom software. PET/MRI data were collected with an energy window of 350–650 keV. No attenuation, random coincidence, scatter or dead-time corrections were applied to PET/MRI datasets (All data were collected at count rates low enough to avoid significant effects from dead-time). Images were reconstructed with a 3D maximum *a posteriori* (MAP) algorithm (30 iterations, $\beta = 1 \times 10^{-5}$) [60]. Detector sensitivity normalization was incorporated into the forward model in MAP reconstruction. The FOV of reconstructed PET/MRI scanner images is $35.4 \times 35.4 \times 12.8 \text{ mm}^3$. Image matrix dimensions were $128 \times 128 \times 17$ and voxel size was $0.28 \times 0.28 \times 0.75 \text{ mm}^3$. The average spatial resolution of the scanner (mean of values measured at off-axis distances of 0, 5, 10 mm using filtered back-projection reconstructed images) is 1.5 mm [198].

3.4.3.2 Phantom Studies

We measured the linearity and uniformity of reconstructed image intensities from the PET/MRI scanner. A linearity phantom was constructed by evenly spacing four 1 mL syringes (Becton Dickinson, BD, inner diameter = 4 mm) on the inner surface of a 50 mL Falcon tube (diameter = 30 mm, BD, figure 3.21). Syringes were filled with ^{18}F -FDG at concentrations of 2.5, 1.3, 0.63, and 0.31 MBq/mL, as measured by a well counter (CRC-15R, Capintec). The phantom was centered in the PET FOV and imaged simultaneously with PET/MRI 9 times over 2 hours (PET: duration = 720 s; MRI: FLASH TR/TE = 500/4 ms, FOV: $35.4 \times 35.4 \text{ mm}^2$, slice thickness = 0.75 mm, matrix size = 128×128 , 40 slices).

The phantom was rotated 90° clockwise about the long axis of the system between each scan to test for activity-dependent differences in response among different regions of the reconstructed images. Response homogeneity within PET images was measured with a “hot rod” phantom configured with the same geometry as the linearity phantom, except that all syringes contained 1.5 MBq/mL of ^{18}F -FDG. The hot rod phantom was imaged 10 times over 2 hours (PET: 600 s) with a 90° clockwise rotation between consecutive scans. The first linearity phantom scan of the study ses-

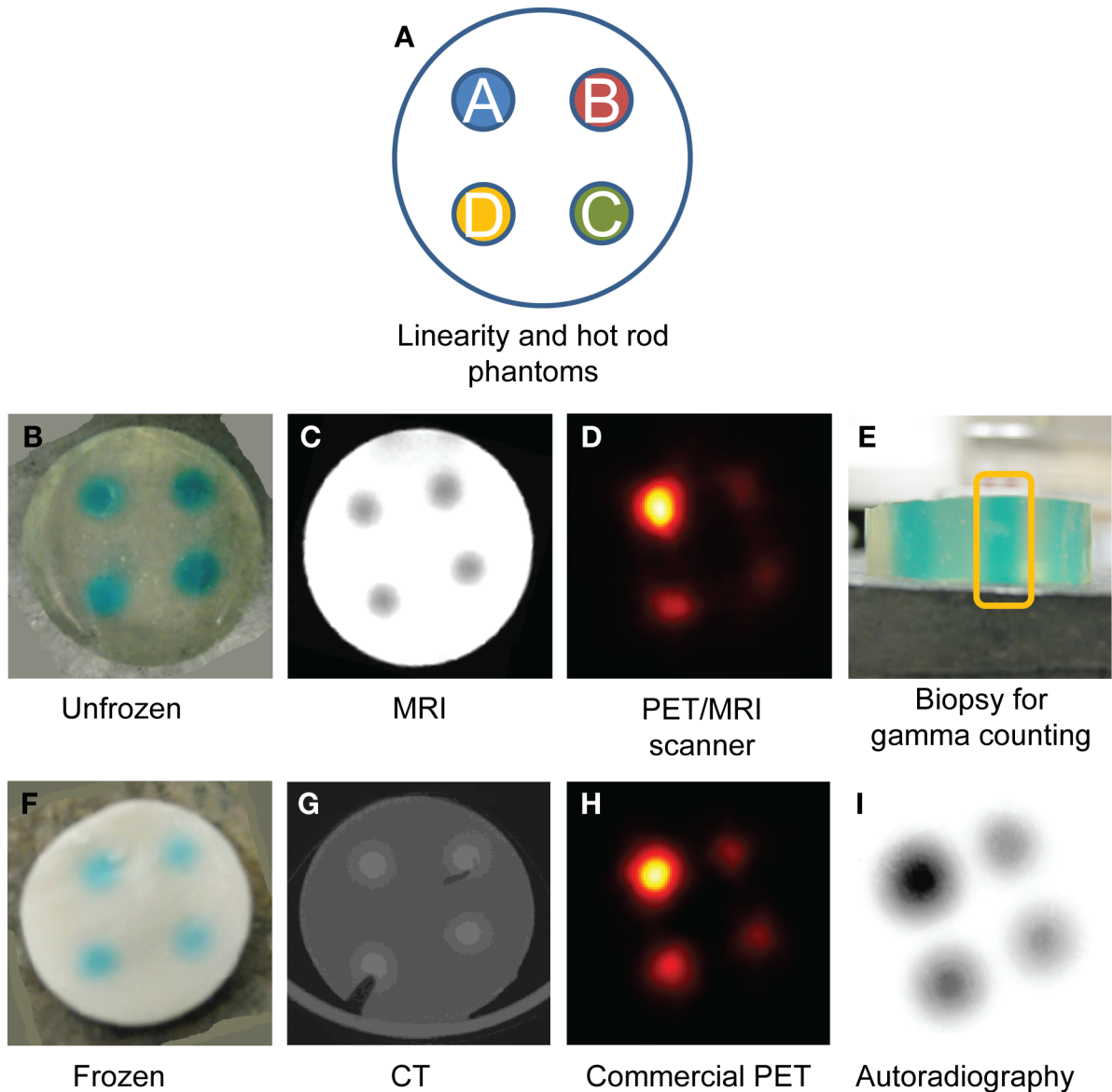


Figure 3.21: Phantoms used in this study. (A) Schematic of the linearity and hot rod phantoms (syringe and gelatin) used in the study. (B)–(I) Images of gelatin linearity phantoms acquired across modalities. Blue food dye was used to visualize rods (B,F), while MR (Prohance) and CT (Isovue 300) visible contrast agents were mixed with radioactivity to enable visualization in MRI and CT respectively (C,G). A small crack is evident in a frozen test phantom prepared for CT imaging (G); this phantom was not used in the studies. The physical properties of the gelatin phantom (E) enabled sampling for gamma counting as well as thin, frozen sectioning for autoradiography (I). The orange box in (E) outlines a rod that was sampled with a biopsy punch and transferred for weighing and gamma counting.

sion was used to derive regression coefficients with which other scans were calibrated; this method incorporated phantom-specific compensation for attenuation, scatter and partial volume effects. Detailed description of the calibration procedure is given in section 3.4.7.1.

We also validated stability of the PET/MRI scanner over multiple imaging sessions. Linearity phantoms were prepared and imaged as described above for 3 separate imaging sessions over 10 days. The coefficient of variation (CoV) of calibration coefficients across sessions were calculated.

3.4.3.3 Animal Studies

Animal studies were approved by the Animal Care and Use Committee at Caltech. Ten days prior to imaging, TgCEA⁺C57BL/6 mice were implanted in the right flank with 8×10^5 MC38.CEA colorectal adenocarcinoma cells [199].

¹⁸F-FDG. A tumor-bearing mouse was fasted for 4 hours, injected intravenously (i.v.) with 37 MBq of ¹⁸F-FDG, then warmed and sedated with a 1.5% isoflurane/air mixture. The injected activity was sufficient to allow imaging of the same mouse by PET/MRI, microPET and QAR in the same study session. After 60 min, the mouse was euthanized and secured to a cardboard platform; mouse and platform were placed on a custom-designed plastic holder. The mouse was positioned with its long axis orthogonal to the transaxial imaging planes of the PET/MRI scanner and imaged unfrozen with simultaneous PET/MRI (PET: 600 s; MRI: RARE TR/TE = 3500/4.5 ms, matrix size = 128 × 128, resolution = 0.28 × 0.28 mm², slice thickness = 0.75 mm, 34 slices). Following the initial PET/MRI scan, the mouse was frozen in a dry ice and isopropyl alcohol bath, repositioned into the holder and reimaged (PET: 1200 s; MRI: same as above). Using recorded prompts count rate and previous work relating prompts rate to true coincidence count rate for the PET/MRI scanner [198], we estimated the true-to-prompt coincidence event ratio for our scans to be ~50–75%.

To facilitate a) shielded transport between the laboratories where PET/MRI and microPET/autoradiography experiments were done; and b) cryosectioning for autoradiography, the frozen mouse was cut to obtain a 3.5 cm long section axially-centered on the tumor. A laser guide ensured that the cut face was orthogonal to the long axis of the mouse. The section was positioned in an imaging holder parallel to the holder's axis to ensure that the cut-face was orthogonal to the long axis of the microPET R4 scanner (Concorde Microsystems) [200]. The mouse section was

then serially imaged with microPET and microCT (Siemens InveonCT) (PET: 1200 s, 350–650 keV energy window, 6 ns timing window, corrections made for detector normalization, dead-time and random coincidence events, CT: 80kVp, 500 μ A, 200 ms/step, 361 steps covering 360°, 2 axial bed positions with a 20% overlap, voxels binned \times 4). Measured true-to-prompt event ratio in all microPET scans were >99%. MicroCT images were reconstructed with the COBRA-3D reconstruction algorithm (Exxim) to produce datasets with isotropic voxels (210 μ m per side). Prior to reconstruction, microPET list-mode data were truncated to contain the same number of prompt coincidence events as in the PET/MRI frozen-state scan. This was done in order to make true count densities at least roughly comparable in the PET/MRI and microPET scans. Images were then reconstructed using 3D OSEM-MAP (3D OSEM: 4 iterations, 12 subsets, followed by MAP: 30 iterations, $\beta = 0.33$, optimized for uniform resolution).

After microPET imaging, the mouse section was embedded in a 4% carboxy-methyl-cellulose (Sigma-Aldrich) water mixture within a custom-steel mold. The mold was placed in a dry ice and isopropyl alcohol bath for 10 minutes and then into a -20°C freezer for 1 hour before mounting onto a cryomicrotome (Bright 5030/WD/MR, Hacker Instruments). Slices were removed until tumor tissue was apparent. After that, 50 μ m thick transaxial frozen sections, spaced 250 μ m apart, were acquired for autoradiography until all tumor tissue had been sectioned, ensuring at least 3 autoradiography slices per PET/MRI image slice. During sectioning, the block face was photographed (Nikon D70, Tamron 90 mm 1:2.8 Macro ϕ 55 lens). Sections were placed onto storage phosphor screens (Super Resolution Screen, PerkinElmer). A ^{14}C standard strip (Amersham) was placed on each screen for calibration of screen sensitivity. Screens were exposed to collected sections for 3.5 days at -20°C and then read with a laser scanner (Packard Cyclone).

^{64}Cu -labeled Antibody. Distribution of a radiolabeled antibody against CEA, ^{64}Cu -DOTA-NHS-M5A (9), was imaged in a tumor-bearing mouse. The antibody (5.6 MBq, specific activity = 0.37 MBq/ μ g) was injected i.v., and *in vivo* simultaneous PET/MRI imaging was performed at 4 and 20 hours post injection. The animal was kept at 35°C – 37°C with a warm air flow. At each timepoint, PET (3600 s); anatomical MRI (RARE, same parameters as above) and diffusion MRI images (TR/TE=3000/25ms, matrix size = 128×128 , resolution = $0.28 \times 0.28 \text{ mm}^3$, slice thickness = 0.75 mm, 10 slices, $\delta/\Delta = 7/14\text{ms}$, b-values = 0, 300, 1000 s/mm^3 , 1 direction) were acquired. The mouse

was sacrificed 24 hours post injection. Images were then acquired with the PET/MRI scanner, microPET and autoradiography and processed as per the ^{18}F -FDG experiment.

3.4.3.4 Image Analysis

Image Coregistration. PET/MRI scanner images were aligned with MRI as previously described [201]. Images from non-frozen and frozen specimens were aligned using a rigid-body transformation obtained via landmarks along the anatomic contour. MicroPET and microCT images were coregistered with a rigid-body transformation (Amira) using landmarks present on both images. Autoradiography images acquired from different phosphor screens during the same study session were cross-calibrated using ^{14}C standard strips. For animal studies, slices within each autoradiography and photography image z-stacks were first aligned across the stack using the Fiji StackReg function (<http://pacific.mpi-cbg.de/wiki/index.php/Fiji>). The two stacks were then coregistered using a rigid-body transformation derived from 12 landmarks per slice clearly seen on both stacks. Three adjacent slices falling within a given PET slice were averaged to match the slice thickness of the PET/MRI scanner. Prior to cross-modal registration, PET/MRI and autoradiography/photography datasets were resliced to 1.2 mm thickness to match the slice thickness of reconstructed microPET images. Finally, PET/MRI and microPET/microCT image stacks were aligned to the autoradiography/photography stack using a landmark-based rigid-body algorithm implemented in MATLAB, resulting in a coregistered combined dataset with voxel dimensions of $0.28 \times 0.28 \times 1.2 \text{ mm}^3$.

Regions of Interest. For phantom images acquired in PET/MRI studies, cylindrical volumes of interest (VOIs) were axially centered within images of rods (diameter = 40% of the rod, length = 8.3 mm). Tumor and whole-animal VOIs were drawn on photographic stacks using MRICro (<http://www.MRIcro.com>) and applied to PET and autoradiography images.

PET/autoradiography Comparisons. Similarity metrics used to compare animal images are summarized in table 3.10. Image intensities within VOIs were scaled to fall between 0 and 1 for similarity analysis. We used scaled images because it was not feasible to perform autoradiography of a linear calibration phantom during day-long animal imaging experiments. Scaling was valid since phantom studies showed that the PET/MRI scanner, microPET and autoradiography response

were linear (see section 3.4.7, figures 3.23 and 3.30).

Table 3.10: Image similarity metrics used to compare PET image quality with autoradiography

Metric Name	Equation	Description
Correlation coefficient	$\frac{E[(x-\mu_x)(y-\mu_y)]}{\sigma_x\sigma_y}$	Voxel by voxel correlation between two regions of interest. x, y refer to the voxel value for the first and second image respectively, μ and σ refer to the mean and standard deviation of the voxel values in images X and Y. E denotes expectation value.
Peak signal-to-noise ratio (PSNR)	$10\log_{10}\frac{Max-voxel-value_i \times Max-voxel-value_j}{Mean-voxel-difference_{ij}}$	Voxel by voxel measure of SNR within a ROI between images i and j [202].
Structural similarity index (SSIM)	$SSIM(x, y) = l(x, y)^\alpha c(x, y)^\beta s(x, y)^\gamma,$	Similarity index comparing local image structure. l, c, s refer to the luminance, contrast and structure of the image, respectively. α, β, γ are adjustable parameters. (Default settings from [202] were used.) See reference for a detailed description.
Complex wavelet structural similarity index (CWSSIM)		Same as SSIM, but with wavelet analysis incorporated [203].

***In vivo* PET/diffusion MRI.** Aligned and calibrated (using a linearity phantom as described in section 3.4.7) PET/MRI scanner images were converted to units of percent injected dose per gram (% ID/g). (ADC) tumor maps were generated from diffusion MRI data [192]. Cooccurrence matrix analysis was used to compare ADC and PET images while taking into account the resolution differences between imaging modalities. The cooccurrence matrix C was calculated using the following equation:

$$C_{\Delta x \Delta y \Delta z}(i, j) \sum_{p=1}^n \sum_{q=1}^m \sum_{r=1}^l = \begin{cases} 1, & \text{if } ADC_r(p, q, r) = i \text{ and } PET_r(p + \frac{\Delta x}{a}, q + \frac{\Delta y}{b}, r + \frac{\Delta z}{c}) = j, \\ 0, & \text{otherwise.} \end{cases}$$

ADC_r and PET_r are ADC and PET images whose voxel values have been binned to one of 15 evenly spaced values lying within the intervals $i \in [0, 1.5 \times 10^{-3} \text{ mm}^2/\text{s}]$ and $j \in [0.25d, 0.75d]$ (d is

the maximum % ID/g value in the VOI), respectively. p , q and r are voxel coordinates along x, y and z directions of the $n \times m \times l$ image volume (defined by the VOI). a , b and c are the PET voxel dimensions ($0.28 \times 0.28 \times 0.75 \text{ mm}^3$). The parameters $|\Delta x|$, $|\Delta y|$ ($\leq 1.5 \text{ mm}$) and $|\Delta z|$ ($\leq 2.1 \text{ mm}$) were equated to the image resolution (average FWHM values) of the PET/MRI scanner [198].

Statistical Analysis Two-way ANOVA was used to compare image homogeneity and linearity of PET/MRI scanner phantom data. Differences between rod intensities measured from different quadrants of the image and individual rod intensities measured from separate images during the study session were tested. Differences were considered significant when p -values were < 0.05 .

3.4.4 Results

3.4.4.1 PET/MRI Scanner Response

Activity Concentration Recovery. Activity concentration recovery (ACR = measured value/true value, measured value obtained from images using calibration coefficients derived as described in section 3.4.7.1) from PET/MRI scanner phantom images are shown in figure 3.22. Linearity phantom images had ACRs close to unity (0.97 ± 0.06) for all rods (diameter = 4 mm) across a 10-fold range of activity concentrations. No significant difference in activity concentration recovery among spatial locations ($p = 0.3$) or among different rod activity concentrations ($p = 0.3$) were observed. However, reproducibility of the scanner-derived ACR was inversely related to rod activity concentration (ACR standard deviation = 23% for the lowest activity concentration rod compared to 9% for the highest activity concentration rod). This is likely due to increased noise in reconstructed images at lower activity concentrations. Hot rod phantom images also had ACRs (1.03 ± 0.03) close to unity for a range of activities. Again, no significant dependence of ACRs on spatial location ($p = 0.5$) or rod identity ($p = 0.5$) was seen.

Stability Across Imaging Sessions. Calibration curves and regression coefficients obtained with linearity phantoms from 3 separate imaging sessions over 10 days are shown in figure 3.23. The data show that the PET/MRI scanner has a temporally stable and linear response across a wide range of activity concentrations when system parameters are kept constant.

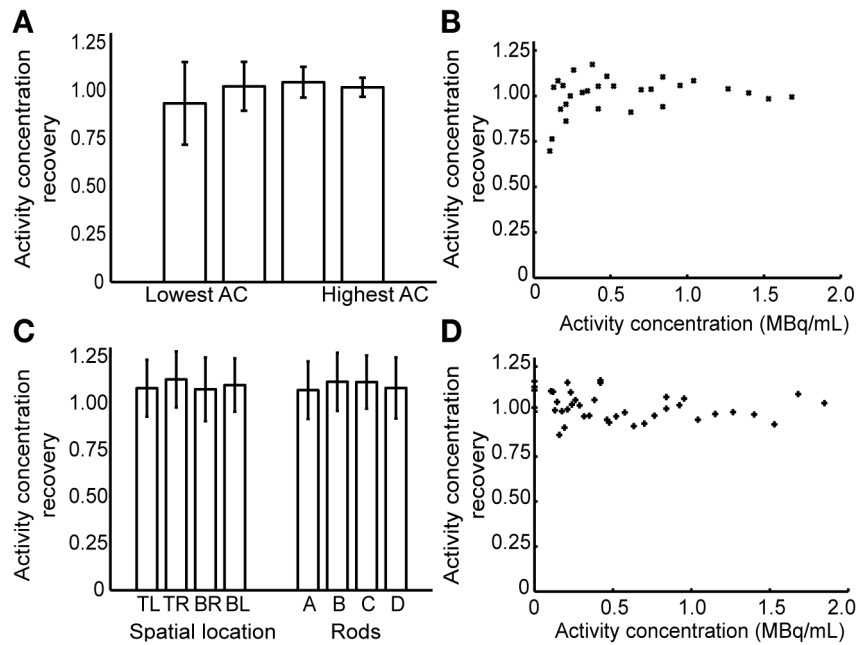


Figure 3.22: PET/MRI scanner accuracy and stability within an imaging session. Measurements were made on syringe “rod” phantoms described in 3.4.3.2. (A) Activity concentration recovery (ACR) for ^{18}F -FDG linearity phantom images acquired over 2 hours, with ROIs drawn over rods with varying activity concentrations. No significant dependence on spatial location ($p = 0.3$) or activity concentration ($p = 0.3$) was observed. (B) Rod ACRs compared with actual rod activity concentrations. (C) ACRs of ^{18}F -FDG hot rod phantom images acquired over 2 hours, compared with respect to spatial location (TL = top left of image FOV, TR = top right of image FOV, BR = bottom right of image FOV, BL = bottom left of image FOV) and rod identity. No dependence on spatial location ($p = 0.5$) or rod identity ($p = 0.5$) was observed. (D) Rod ACRs compared to actual rod activities at the time of imaging. All hot rod syringes contained the same activity concentration. Error bars denote SD.

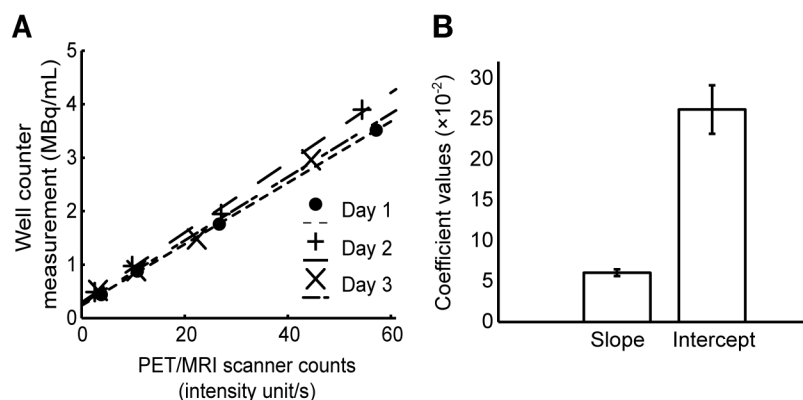


Figure 3.23: Linearity and stability of the PET/MRI scanner across multiple imaging sessions. Measurements were made on syringe “rod” phantoms described in 3.4.3.2. (A) Linearity phantom rod image intensities from 3 separate imaging sessions over the course of 10 days are plotted against actual activity concentrations. Fitted linear regression lines used to determine the calibration coefficients are also shown. (B) Slope and intercept calibration coefficients (mean and SD) across the 3 sessions. CoVs for the slope and intercept were 6.8% and 11% respectively.

3.4.4.2 Comparison of Image Intensity Patterns Across Modalities

Qualitative Assessments. Figure 3.24A shows coregistered images of a mouse injected with ¹⁸F-FDG and imaged using PET/MRI, microPET/CT and autoradiography/photography. As expected, FDG uptake in the tumor was elevated compared to surrounding tissues. The image intensity pattern was heterogeneous within the tumor and approximately congruent among all 3 imaging systems. Regions of high activity were present in lateral and medial lobes of the tumor, with a region of lower activity in between. The central region had somewhat higher relative intensity in autoradiography compared to PET images. Images acquired 24 hours after injection of ⁶⁴Cu-DOTA-NHS-M5A are shown in figure 3.24B. Expected tumor localization of the antibody is observed, along with intratumoral heterogeneity. The multilobed intratumoral uptake pattern is similar across PET/MRI, microPET and autoradiography.

Quantitative Evaluation. Image similarity between different pairs of radioactivity image sets was quantified using several metrics. Comparisons of PET/MRI scanner and microPET R4 with autoradiography are shown in figures 3.25 and 3.26. Pixel-based correlation coefficients for all PET to autoradiography comparisons were moderate to high (>0.7) for both whole-mouse cross sections and tumor ROIs (figure 3.25A–B). Not surprisingly, correlation increased when autoradiography was blurred to match resolution to the PET/MRI scanner and microPET, and dropped nearly to zero

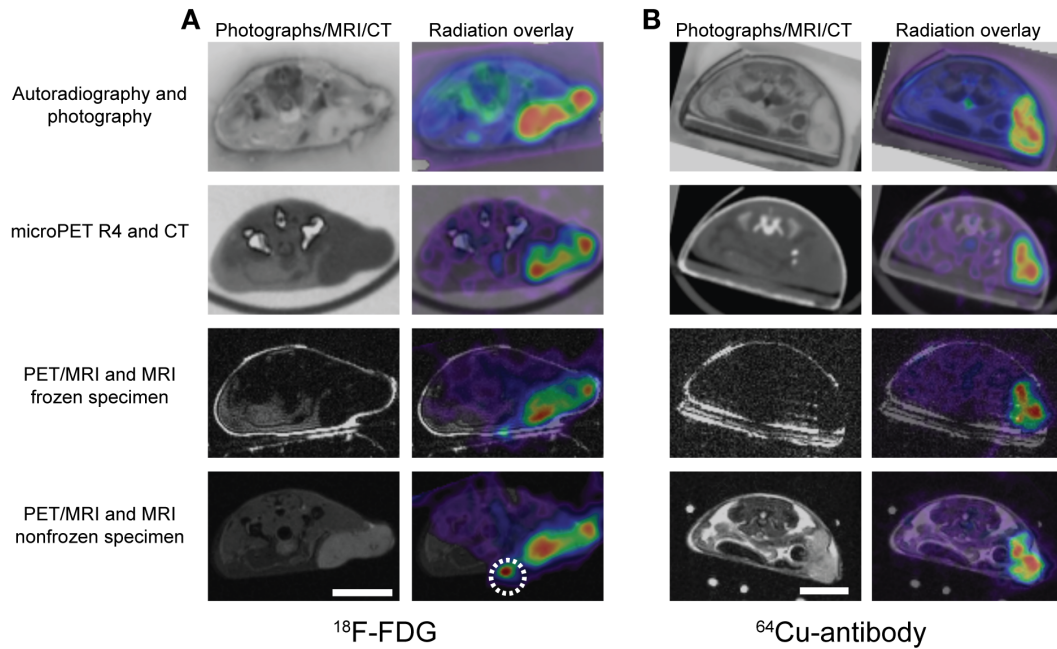


Figure 3.24: Multimodal imaging of radiotracer uptake in tumors. Mice bearing MC38.CEA tumors were injected either with (A) ^{18}F -FDG or (B) anti-CEA ^{64}Cu -DOTA-NHS-M5A antibody and sacrificed after an uptake period. Tumor regions were then imaged with the PET/MRI scanner, frozen, reimaged with PET/MRI, imaged in the frozen state with microPET and microCT, cryosectioned and imaged with autoradiography. Matched tumor slices show qualitatively similar uptake patterns. PET/MRI scanner images of ^{18}F -FDG show a hot spot (circle) not observed with other modalities. Comparison with MRI showed the hot spot to be on the animal's surface, indicating that it was caused by urine residue that was removed prior to subsequent imaging (Scale bar = 10mm).

of PET images for tumor ROIs generally showed higher intermodal similarity than did whole-body ROIs. When autoradiography dataset was scrambled, structure-based comparisons decreased to nearly zero, confirming that the metrics do reflect image similarity. Similarity metrics obtained by comparing PET/MRI and microPET images to autoradiography were highly correlated ($r \geq 0.9$).

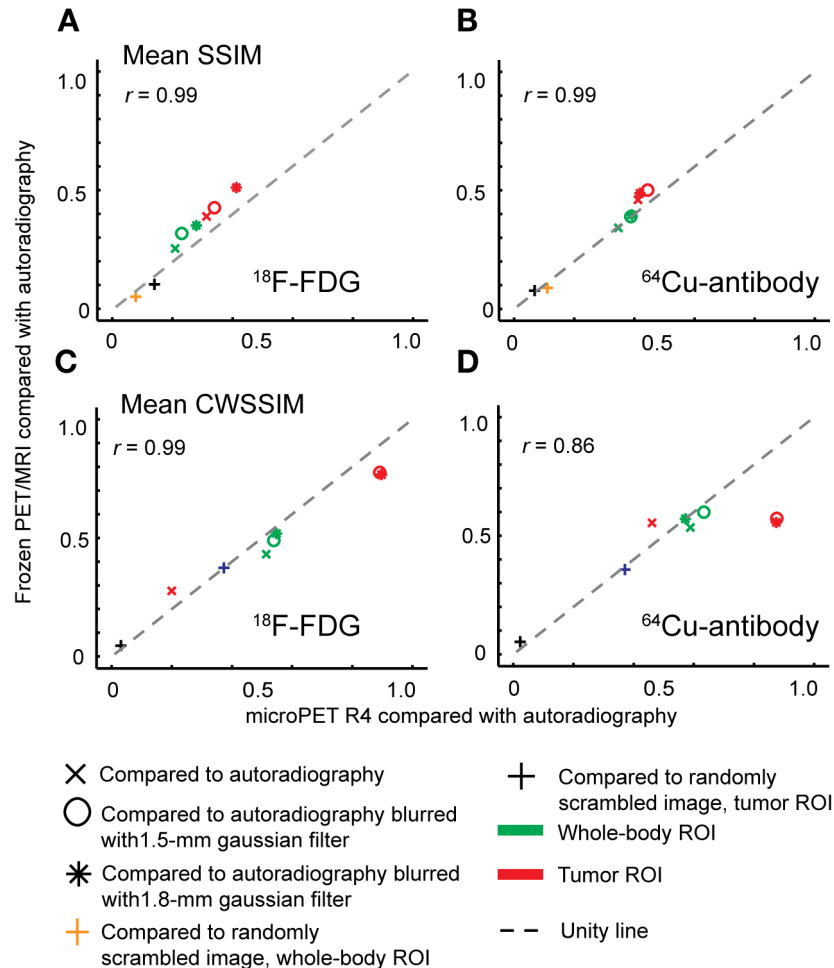


Figure 3.26: Structure-based similarity among PET/MRI scanner (frozen specimen), microPET and autoradiography images. $^{18}\text{F-FDG}$ and $^{64}\text{Cu-antibody}$ coregistered datasets were compared as in figure 3.25, except using SSIM (A–B) and CWSSIM (C–D). Pearson correlation coefficients comparing PET/MRI vs. autoradiography and microPET vs. autoradiography metrics are shown.

Small differences shown by the metrics can be related to images. For example, comparison of FDG data slightly favored the PET/MRI scanner over microPET. A possible explanation for this can be seen in figure 3.24A, where PET/MRI of the frozen specimen and QAR images show a more pronounced low activity region between the two main high activity lobes and relatively flat dorsal tumor contours compared to the microPET image. Differences among modalities are

less pronounced in the antibody images; this is seen in figures 3.25B, D and 3.26B, D, where on average data points lie closer to the identity line than for FDG images. CWSSIM, a metric less sensitive to geometric distortions compared to other metrics [203], attenuates these differences but also indicates better structural agreement between microPET and blurred autoradiography images of ^{64}Cu in tumor compared with PET/MRI.

Simultaneous *In Vivo* PET/MRI. Tumor uptake of ^{64}Cu -DOTA-NHS-M5A at 4 and 20 hours post injection is compared to simultaneously acquired MR-ADC images in figure 3.27. At 4 hours post injection, much of the antibody was still in blood, as shown by the high signal in the inferior vena cava (figure 3.27A) and low uptake within the ventral portion of the tumor. At 20 hours, the antibody signal was spread throughout the tumor parenchyma (figure 3.27B). Cooccurrence matrix analyses of the uptake pattern reflect these observations (figure 3.28). At 4 hours, regions of relatively high antibody concentration within the tumor tended to be in regions with high ADC values, suggesting that the antibodies were in the tumor's intravascular and/or interstitial spaces (figure 3.28A). By 20 hours, this high uptake/high ADC cooccurrence disappeared, suggesting uniform antibody distribution within the tumor (figure 3.28B).

3.4.5 Discussion

Feasibility of *in vivo* PET/MRI has been well demonstrated [190]. However, it remains to be shown that PET images from such a scanner accurately depict activity distribution within the imaged tissue. Here, we demonstrated the ability of a MR-compatible PET scanner [105] to produce quantifiable intratumoral images that are stable, linear and concordant with images from a commercial small animal PET scanner and autoradiography.

PET systems require a uniform and linear image intensity response. PET/MRI scanner-derived images of linearity and hot rod phantoms showed the system to be stable and linear during a single imaging session and across multiple sessions. The linearity phantom allowed us to demonstrate the stability of the PET/MRI system for measuring multiple activity concentrations in the same image across multiple time points within an imaging session. These characteristics are crucial for successful dynamic simultaneous PET/MRI studies. Activity concentration recovery in this study compares well with previous reports for small animal PET [204, 205].

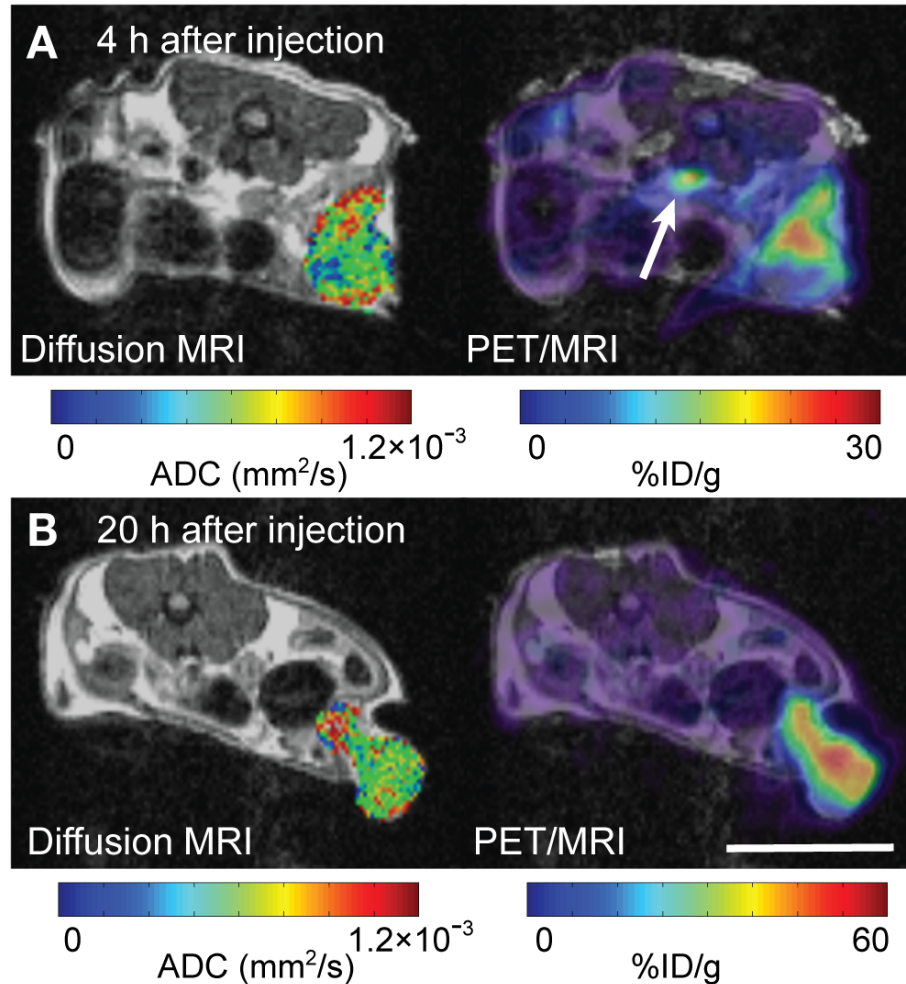


Figure 3.27: *In vivo* simultaneous diffusion MRI/radiolabeled antibody PET reveals phases of antibody uptake. PET/MRI of a mouse was obtained at 4 (A) and 20 (B) hours post injection. Slices from the two time points were matched as closely as possible. Both PET and diffusion MRI show intratumoral heterogeneity of uptake and ADC values respectively. A general accumulation of antibody was observed between 4 to 20 hours. Focal distribution of antibody was observed in the more dorsal portion of the tumor at 4 hours post injection; by 20 hours, the distribution encompassed most of the tumor mass. Spatial patterning of the ADC (shown only for the tumor) was similar at both time points. PET images were calibrated using a linearity phantom as described in section 3.4.7. Arrow points to the inferior vena cava (Scale bar = 10mm).

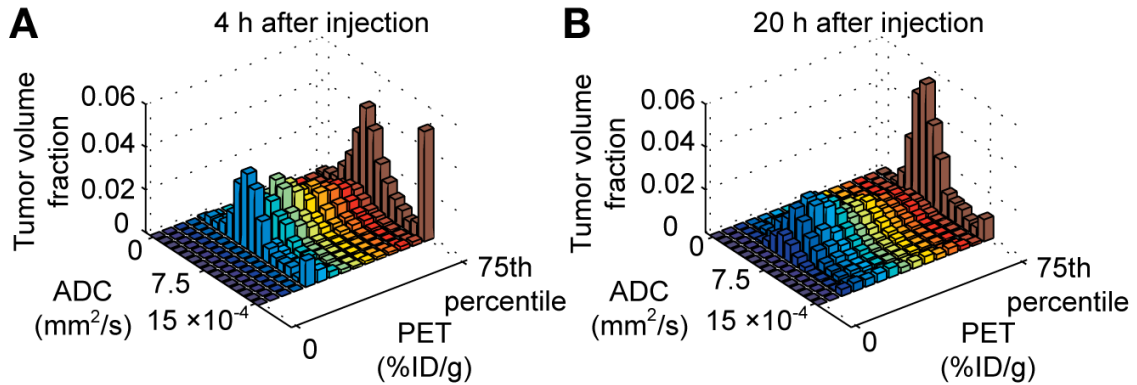


Figure 3.28: Cooccurrence matrix analysis of functional PET and MRI data offers insight into tumor antibody uptake. (A) cooccurrence matrix comparing antibody uptake and ADC values at 4 hours post injection. The uptake comparison window was adjusted to account for the lower spatial resolution of PET (1.5 mm FWHM) compared to MRI. At 4 hours, a large fraction of the antibody signal colocalized with regions of high ADC, ($>0.0015 \text{ mm}^2/\text{s}$) suggesting much of the antibody was in vascular and/or interstitial spaces. (B) By 20 hours, that component had disappeared; the antibody was spread more evenly across the tumor mass. This was not apparent with pixel-by-pixel matching (figure 3.31).

To quantitatively interpret and compare PET and QAR images, image intensities for both modalities need to be linearly related to object activity concentration. To demonstrate that PET and QAR imaging systems used in this study are linear and to confirm that our intended strategy for animal studies is valid, we developed a gelatin phantom that could be visualized by optical imaging, MRI, CT, PET, QAR, and assayed for radioactivity concentration by gamma counting (figure 3.23). Figure 3.30 shows that image intensities derived from phantoms were linearly related to sample activity concentration for all 3 imaging systems, enabling us to compare images from different systems with confidence.

The ability to return images with intensity patterns reflecting actual *in vivo* activity distributions was compared among the PET/MRI scanner, microPET and QAR. intratumoral activity distributions for a metabolic marker (^{18}F -FDG) and a targeted antibody were in good overall spatial concordance among modalities. However, detailed examination of the images revealed some differences. Resolution differences between autoradiography and PET can be seen by the presence of finer structures in autoradiographs compared to their PET counterparts. For example, the antibody distribution in figure 3.24B showed a small rim of relatively high activity in the ventral portion of the tumor autoradiographs not visible with PET. Christian *et al.*, reported similar observations, attributing them

to differences in resolution between PET and autoradiography [206]. Application of a Gaussian filter to autoradiography images acquired in this study support this assertion (figure 3.29). Lack of attenuation and scatter correction in PET/MRI scanner images may also contribute to disparities. Attenuation of 511 keV photons can be as high as 15% with small animal-sized objects [207]. However, since tumors imaged in our experiments were superficial, we expect attenuation-related differences between PET and autoradiography to be minimal. Regardless of the limitations of the imaging techniques used in this study, the intratumoral patterns are qualitatively similar among the PET/MRI scanner, microPET and QAR for both ^{18}F -FDG and the ^{64}Cu -antibody. Furthermore, similarity metrics showed good overall correlation between both PET systems and QAR. Image differences between the two PET systems may be due to resolution differences between the systems and, in case of the ^{18}F -FDG study, high count rates during the PET/MRI scan compared to the microPET.

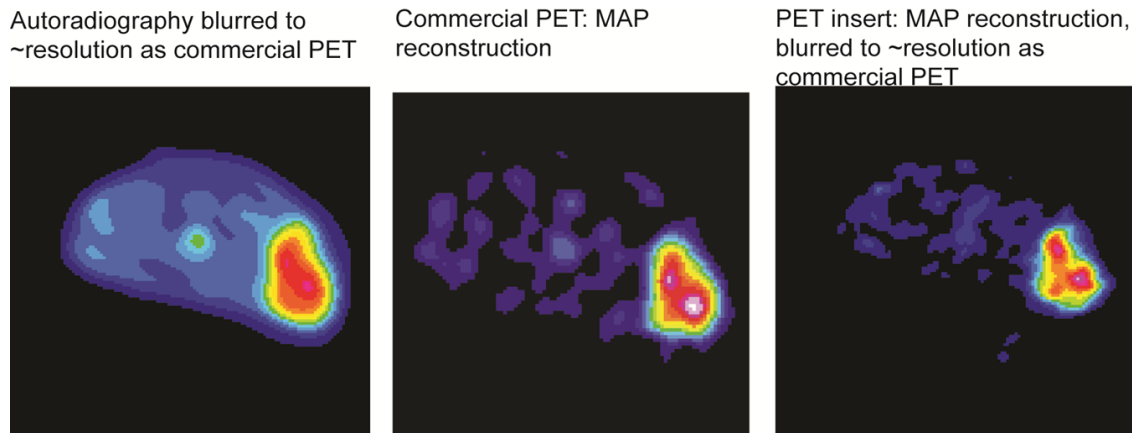


Figure 3.29: Resolution differences between autoradiography and PET. Images from the antibody study used for analysis. 2D Gaussian filters were applied to the autoradiography and PET insert images to simulate the spatial resolution of the commercial microPET R4 (~1.8 mm). Image filtering of the autoradiography and PET insert images improved correspondence to the microPET image. This highlights the resolution differences between the three imaging systems.

The necessity and utility of detailed quantitative analyses are illustrated in figure 3.27. Having demonstrated good spatial fidelity of PET/MRI scanner images, we hypothesized that biological inferences can be made by comparing simultaneously acquired PET and MR images. Fidelity of the PET images allowed us to conclude that there was a time dependent heterogeneous tumor accumulation of antibody during a preliminary study (figures 3.27, 3.28).

Previously, two methods have been employed to compare multimodal intratumoral datasets. Cho *et al.* performed a pixel-wise comparison of PET and DCE-MRI maps [183], while Metz *et al.* used arbitrary thresholds to segment tumor subregions for comparison [195]. The former approach neglects differences in resolution between the imaging modalities, while the latter requires multiple PET datasets and is observer dependent. We accounted for differences in resolution between PET and MRI by analyzing image sets with a cooccurrence matrix bin-offset equal to the mean FWHM of the scanner. This analysis demonstrated spreading of antibody from a highly intravascular/extracellular region throughout the tumor. There is recent interest in modeling tumor growth kinetics using multimodal imaging datasets on a pixel-by-pixel basis [208]. The cooccurrence matrix method can be incorporated into these analyses to account for resolution differences between the different modalities. Further improvements can be made to this method. For instance, one can vary the FWHM window to account for varying spatial resolution within the PET FOV. Further considerations of the method is explored in appendix C.

To date, few studies have been published that evaluate PET image fidelity to actual *in vivo* activity distributions. Christian *et al.* developed a Styrofoam holder surrounding a mouse to allow coregistered PET and autoradiography [112]. Cho *et al.* developed a foam mold/plastic holder for rat imaging [183]. The current PET/MRI scanner is not large enough to accommodate these solutions. Instead, landmarks visible on all anatomical images (MRI, CT, photography) along with laser-guided positioning of the mice allowed effective coregistration between PET and QAR.

It is remarkable that, despite limitations inherent in a first-generation prototype (e.g. low sensitivity and lack of random coincidence or dead-time corrections), the current PET/MRI scanner, operated simultaneously with MRI, provided PET images with essentially equivalent spatial patterns as the well-established microPET R4. This demonstrates the ability of the MR-compatible PET scanner to deliver useful *in vivo* information acquired simultaneously with MRI. Next generation systems will likely improve on the quantitative ability and image quality observed in the current system. Methods developed here can be utilized as a benchmark to assess image quality of future systems. Further, availability of good fidelity, coregistered PET/MRI datasets and their QAR/photography counterparts offers the opportunity to explore the biological implications of complementary imaging information, and provide a test bed to develop and evaluate *in vivo*-relevant

PET partial-volume, motion-correction and attenuation-correction algorithms.

3.4.6 Conclusions

We evaluated the ability of a MR-compatible PET scanner to generate spatially and quantitatively accurate images. Images acquired from tumor-bearing mice using different radioisotopes showed good correspondence among the PET/MRI scanner, microPET R4 and autoradiography. A co-occurrence matrix method enabling effective comparison of complementary PET and MR images was presented. This work provides a basis for pursuing biologically relevant simultaneous PET/MRI studies. Progress in hybrid PET/MRI technology will provide improvements in image quality. Methods from this study can be applied to evaluate such improvements.

3.4.7 Supplemental Data

3.4.7.1 Materials and Methods

Calibration of PET/MRI Scanner Images. PET/MRI scanner images of syringe phantoms were decay corrected and normalized for scan duration prior to analysis. The first linearity phantom image acquired during a given study session was used to convert image intensities to units of absolute activity concentration (kBq/mL). Rod image intensities from the PET/MRI image, obtained from cylindrical volumes of interest axially centered on each rod (diameter = 40% of the rod diameter, length = 8.3 mm), were plotted against activity concentrations measured by well counting of samples taken from the phantom. Plots were fitted by linear regression, taking into account the random variability of both the measured independent and dependent variables [209]. The resulting regression coefficients were used to calculate activity concentrations for all images acquired during the corresponding study session. This calibration procedure incorporates phantom-specific compensation for attenuation, scatter and partial volume effects into the calibration coefficients.

Cross-comparison of PET/MRI Scanner and microPET Linearity with Autoradiography and Direct Assay. To enable quantitative comparison of images across PET and QAR systems, it was necessary to ensure that all three systems had a linear response. Two phantoms were used for this purpose. A linearity phantom was made by solidifying a 10% gelatin solution (solid state density =

1.01 g/mL) in a cylindrical mold made from a 50 mL Falcon tube (BD). While the gel was liquid, 4 rods, each 4 mm in diameter, were evenly spaced in the mold. Once the gel had set, the rods were removed, and the holes were filled with gelatin mixed with $^{64}\text{CuCl}_2$ solution (Washington University School of Medicine) containing Prohance (Bracco; 0.1 mM) and Isovue 300 (Bracco; 1mM). Initial mixture activity concentrations were 3.7, 1.9, 0.93, and 0.56 MBq/mL. The 12.7 h half-life of ^{64}Cu enabled the phantom to be imaged on the same day with the PET/MRI scanner, commercial small animal PET and QAR. A second “hot rod” gelatin phantom was made in the same manner as the linearity phantom, except that the 4 rods each contained an initial activity concentration of 1.9 MBq/mL. The rods were surrounded with gelatin containing 0.19 MBq/mL of ^{64}Cu .

Phantoms were cut to 15 mm length to remove gelatin spillover at the ends. The removed sections of the phantom were sampled with a biopsy punch (inner diameter = 2 mm, Miltex), and the samples were placed in pretared Eppendorf tubes for gamma counting. Each region of interest (background and rod regions) was sampled twice. The phantoms were imaged simultaneously with PET/MRI (PET: 2700 s; MRI: FLASH TR/TE = 500/4ms, FOV: $35.4 \times 35.4 \text{ mm}^3$, slice thickness = 0.75 mm^2 matrix size = 128×128 , 40 slices). Immediately after imaging, the phantoms were placed in a dry ice and isopropyl alcohol bath for 5 minutes. The phantoms were subsequently imaged on a microPET R4 (Concorde Microsystems) for 20 minutes (350–650 keV energy window, 6 ns timing window).

After microPET imaging, the phantoms were cut in half. One half was sampled for gamma counting, while the other half was mounted onto a cryomicrotome (Bright 5030/WD/MR, Hacker Instruments). Five $50 \mu\text{m}$ thick frozen transaxial sections, spaced $250 \mu\text{m}$ apart, were obtained and transferred onto a chilled autoradiography cassette containing a storage phosphor screen (Super Resolution Screen, PerkinElmer). The loaded cassette was stored for 1 day at -20°C . Screens were read with a laser scanner (Packard Cyclone). Tubes containing phantom samples were assayed for radioactivity using a calibrated gamma counter (Model 1480 Wizard 3^o, Wallac Oy). Sampling of the phantom was done at each stage of the imaging procedure (PET/MRI imaging, microPET R4 imaging and autoradiography) to account for diffusion of the radioactivity and contrast agent as evident in figure 3.21.

PET images were reconstructed and analyzed as described in section 3.4.3.4. Circular ROIs (diameter = 80% of rod diameter) were used for rod analyses on autoradiography images. Background activity was analyzed with ROIs (diameter = 5.3 mm) placed at five different locations per slice. Although variable slice thickness is a potential source of error in QAR, it was found to be negligible in our study. The CoVs of activity concentrations measured across several slices of the gelatin hot rod phantom (background = 0.19 MBq/mL, rods = 1.9 MBq/mL) were 3.0% and 3.2% for background and hot rod regions respectively. These values are lower than observed by Christian *et al.* (3.5%) after adjustment for differences in slice thickness [210].

Rod and background intensity values from gelatin phantom images were plotted against activity concentrations measured by direct weighing and gamma counting of relevant samples. Plots were fitted by linear regression. Pearson correlation coefficients compared to gamma counting were also calculated.

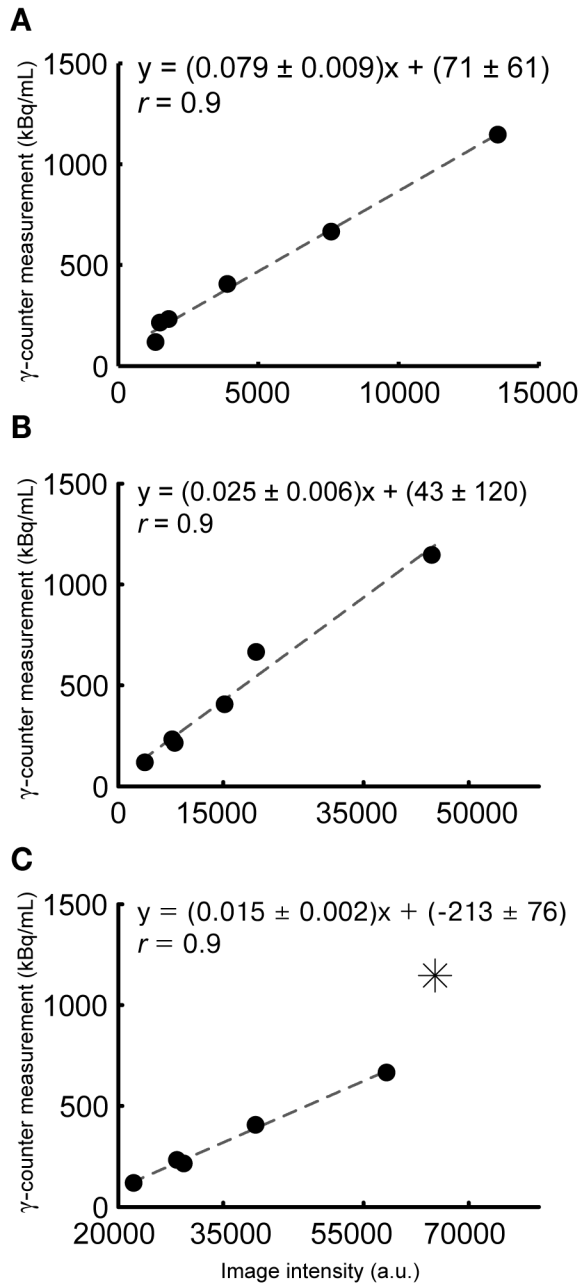


Figure 3.30: Linearity of PET/MR scanner, microPET R4 and autoradiography. Image intensities acquired from the same gelatin-based linearity and hot rod phantoms were plotted against direct assay measurements for (A) PET/MR scanner, (B) microPET R4 and (C) autoradiography. Linear regression was performed for each dataset. Pearson correlation coefficients are shown for each dataset. Software processing revealed that the linearity phantom rod with the highest activity was overexposed on the autoradiography phosphor imaging plate (the * data point in C). That data point was excluded from further analysis. (a.u. = arbitrary units)

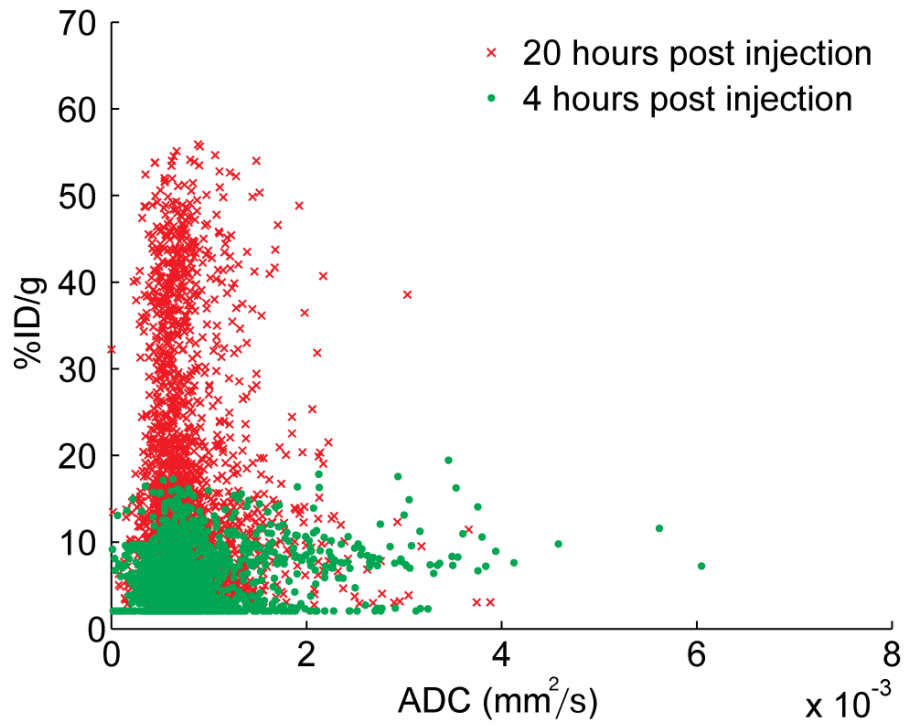


Figure 3.31: Scatter plot of simultaneous diffusion MRI and PET antibody measurements at two different times after injection of ⁶⁴Cu-labeled antibody. Quantitative pixel values from the tumor ROIs shown in figure 3.27 show low correlation between antibody uptake and ADC values ($r = 0.21$ and -0.02 at 4 and 20 hours, respectively).

3.5 Synchronization of PET/MRI Hardware

Simultaneous PET/MRI instrumentation enables PET and MRI images to be acquired in spatial and temporal coregistration. The issue of spatial coregistration of PET and MRI information was addressed in sections 3.2 and 3.3. Here, we address the issue of accurate temporal synchronization of the PET insert and MRI. We describe a system to allow synchronous PET/MRI data acquisition.

A schematic showing how the workflow for synchronous PET/MRI acquisition is shown in figure 3.32. Software modules were inserted into the PET acquisition program and MRI pulse sequence to allow cross-communication of the two systems. The modules can either trigger the process of synchronization or wait for a signal from the other signal. The user can begin acquisition via a PET or MRI trigger.

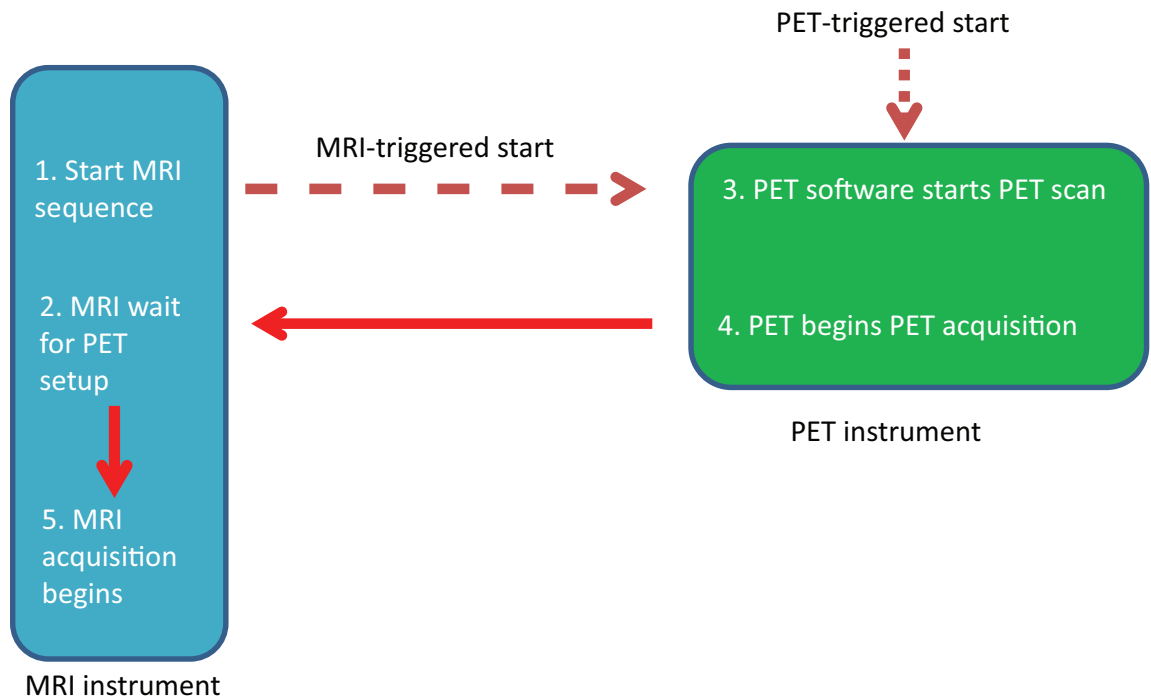


Figure 3.32: Synchronous PET/MRI acquisition may be dictated by either PET or MRI acquisition. Software modules embedded in the MRI and PET programs are written to allow cross-communication between the two systems. PET acquisition can be started by a MRI trigger embedded in an MRI pulse sequence or manually. The PET software then sends a sync signal back to the MRI, allowing the pulse sequence to begin acquisition at a fixed time. Each arrow (except between step 2 and 5) represents a synchronization signal.

Acknowledgment: Thanks to Martin Judenhofer for help with PET software coding. An updated version of the PET software including the module can be obtained on request.

3.5.1 Materials and Methods

3.5.1.1 PET setup

The current PET hardware utilizes the NIM standard, while the input/output of both the MRI system and the PET computer system are based on TTL. A logic level translator (Phillips Scientific, NIM model 726) was used to allow cross-communication between the NIM and TTL standards. The current PET software [162] was modified to enable system cross-communication using TTL via pins available on a standard parallel port.

3.5.1.2 MRI setup

Paravision 5.1 (Bruker, MA) software is used for MRI control. Communication with other systems can be achieved via TTL ports on the MRI hardware console. A software module that can be inserted at the beginning of any Bruker MRI pulse sequence was written to enable cross-communication with the PET system.

The code for the pulse sequence modules, implemented here for a standard FLASH sequence, is shown in appendix D.

3.5.2 Discussion

Temporal synchrony of PET and MRI data is an integral advantage of simultaneous PET/MRI systems. For many PET/MRI applications, the synchrony required are on the scale of the study session (e.g. ~minutes/hours). In these cases, temporally registered PET/MRI datasets can simply be acquired separately in the same study session.

A need for a higher degree of synchrony (~seconds) arises when the physiological processes being studied are transient (e.g. BOLD responses can change within seconds) and when the contrast agents being imaged have fast kinetic properties (e.g. Gd-DTPA or ^{18}F -FDG, section 3.33). Perfect (within milliseconds) synchronization of PET and MRI in these cases facilitates the posthoc analysis of the dual-dynamic datasets.

Further, the availability of temporally aligned data is also beneficial for improving the quantification of PET images. Posthoc MR-guided correction of PET datasets, such with the use of

MR-navigator echoes to reduce motion blurring in reconstructed PET images [100] require that the MRI and PET data be synchronized.

In summary, a system was implemented to enable perfect synchrony of PET and MRI data acquisition for the integrated small animal PET/MRI scanner. All or parts of the system can be easily ported to future versions of the scanner.

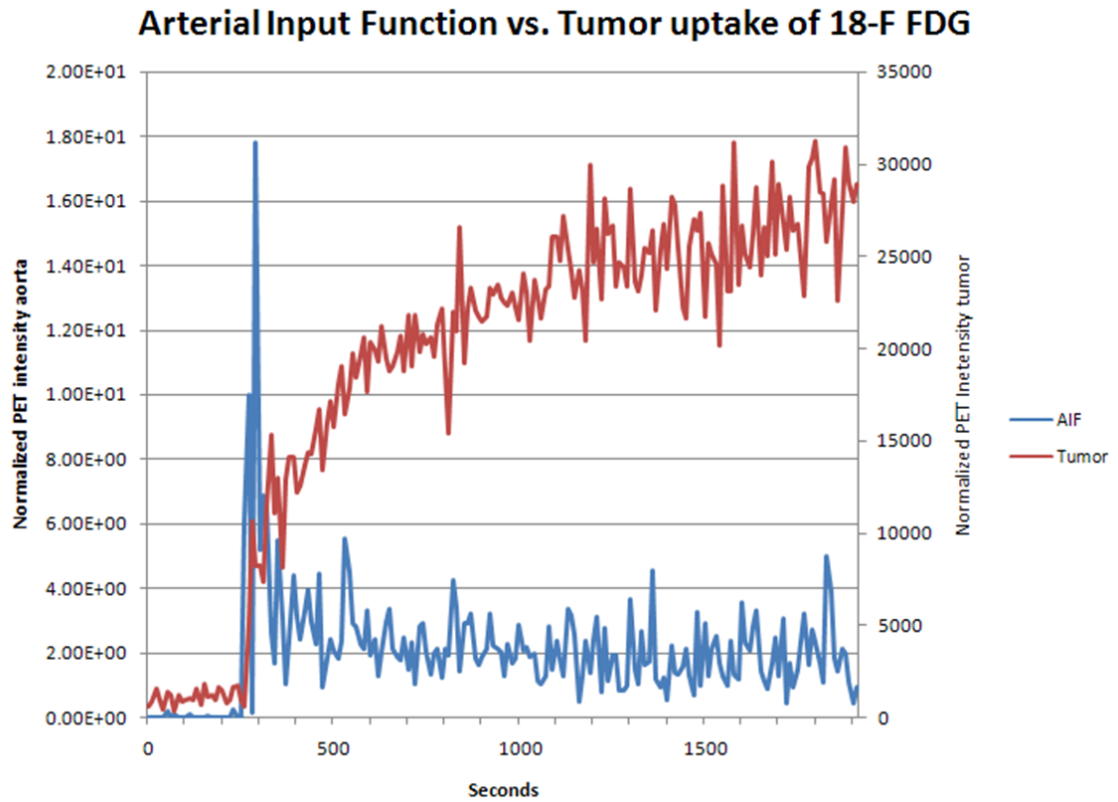


Figure 3.33: Fast kinetics of small molecular agents necessitate synchronous PET/MRI. Time curves of ^{18}F -FDG uptake in the abdominal aorta (AIF) and tumor in a tumor-bearing mouse. The ROI for the obtained time curves were defined by spatially coregistered MRI. Perfect temporal synchrony of such datasets with DCE-MRI will facilitate kinetic modeling and comparisons of multimodal datasets.

3.6 MR Gradient Effects on the PET Insert

In section 3.4, we demonstrated that the PSAPD-based MR-compatible PET system show good quantitative fidelity when used simultaneously with the MRI. However, initial studies with the current PET insert did show a slight decrease (7%–10%) of count rates in the presence of MRI pulse sequences [105]. It is important to understand the effect of such observations as next generation hybrid PET/MRI systems are being developed. Peng [142] explored the effect of MR-gradient switching using a single PET module. They found that count rate attenuation using a single PET detector was related to the location of the detector in relation to the gradient being operated, the magnitude of the gradient waveform and the ramp-time of the gradient. Here, we present results further examining this effect using an intact PET system.

3.6.1 Materials and Methods

Studies were performed using the MR-compatible PET insert. A ^{68}Ge cylindrical source (PET 2.5 C6/0.5, Sanders Medical) was placed in the center of the PET FOV inside a standard RF coil at the center of the MRI FOV. The PET insert was powered as per the conditions described in 3.4. PET data were acquired using in-house software [162]. Each dataset was acquired with a buffer size of 5 K and a duration of 300 s.

To examine the effects of individual MRI pulse sequence components on count rates, data acquisition was performed during trapezoidal/sawtooth waveforms set along the Y gradient direction (TR = 500 ms, no RF pulse was applied). By using electronic TTL gating signals programmed into the pulse sequence, count rates during specific portions of the pulse sequence were examined (figure 3.34):

1. Gradient off
2. Data acquired during the whole sequence (“Combined”)
3. Gradient on (Set at 20% of the maximum magnitude)
4. During ramping (50 ms risetime)
5. During ramping (10 ms risetime)

6. During ramping (1 ms risetime)

Decay and duration normalized counts were compared between portions. Three datasets were acquired for each portion. The global coincidence counts as well as the coincidence counts per detector were recorded. ANOVA with Bonferroni correction was used to analyze the counts data. The peaks and FWHM for energy spectra of each detector were analysed with Kruskal-Wallis test. No thresholds were applied to the spectra.

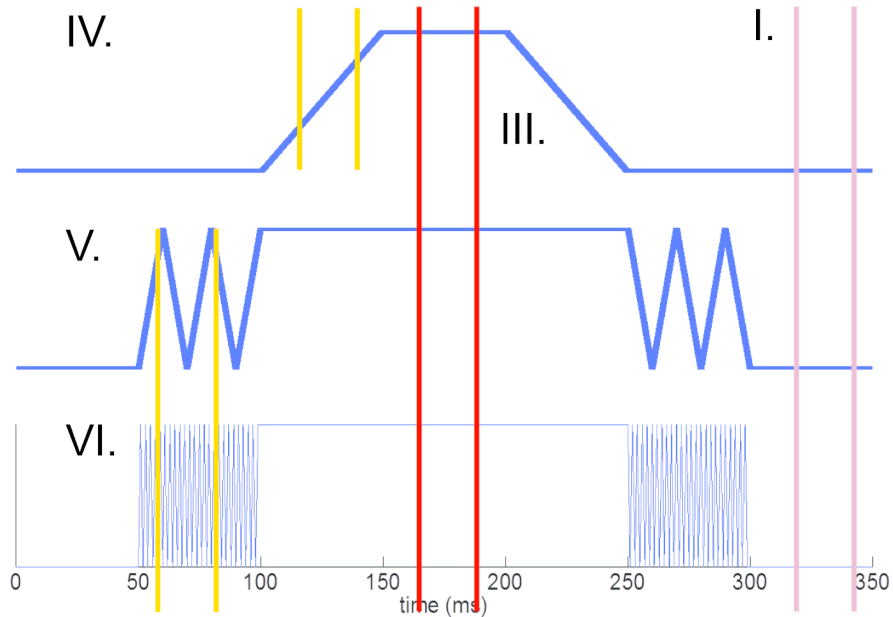


Figure 3.34: MRI gradient effects on count rates. A schematic of different pulse sequences used to probe gradient effects on PET insert count rates. PET data were acquired at different portions of the gradient waveform. I. When the gradient was off, II. during the whole pulse sequence, III. when the gradient is on (here set at 20% of maximum magnitude), during the gradient ramping with a risetimes of IV. 50 ms, V. 10 ms and VI. 1 ms. Pulse sequences were set with a TR = 500 ms. Acquisition windows were done within 50 ms (i.e. vertical bars were truncated to clarify the regions, rather than reflecting the exact timing).

3.6.2 Results

Count rates across all portions are shown in figure 3.35. Consistent with previous results, count rates were highest when the gradient was off. In the presence of gradient power, global coincident counts were attenuated ($p = 0.06$) by 2%–8%. The greatest attenuation occurred during rapid oscillation of the gradient (1 ms risetime, ~8% decrease). Steady-state gradient powering and slower risetimes showed similar attenuation (~2%–4%). Gradient effects on individual detector counts are shown in

figure 3.36. Different count rates across detectors were observed due to the different amplification gains for individual PSAPDs. Count attenuation due to different portions of the gradient waveform on each detector reflects global observations, with the 1 ms risetime showing the greatest decrease. In general, no statistically significant interaction between gradient portions and detector locations was observed ($p = 1$). However, examination of the individual detectors counts versus gradient portions data by one-way ANOVA revealed the detectors that showed significant or close to significant decreases during gradient oscillations were those aligned along the Y gradient direction (quadrant II and IV in figure 3.37, table 3.11). This is consistent with previous results obtained with a single detector.

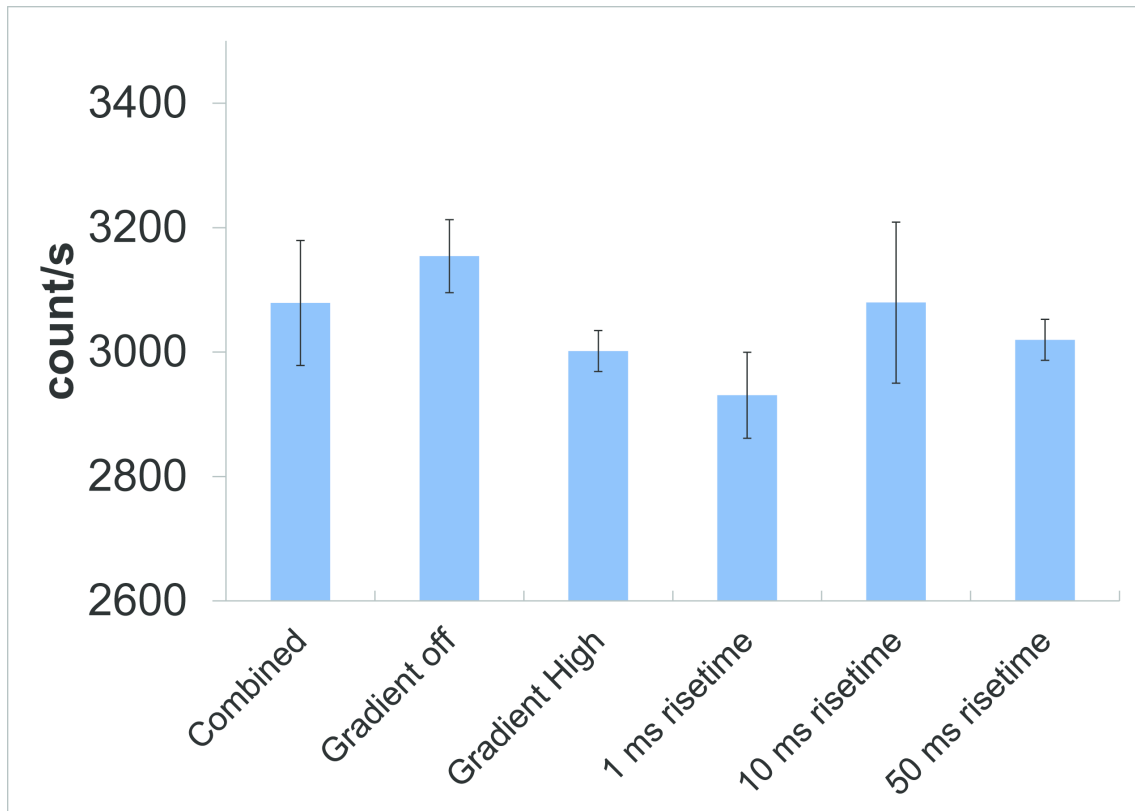


Figure 3.35: MRI gradient effects on count rates for the PET insert. Global coincident count rates for the PET insert under different gradient conditions are shown. No significant differences were observed. However, the presence of the gradient appears to attenuate the count rate slightly. Error bars are SD.

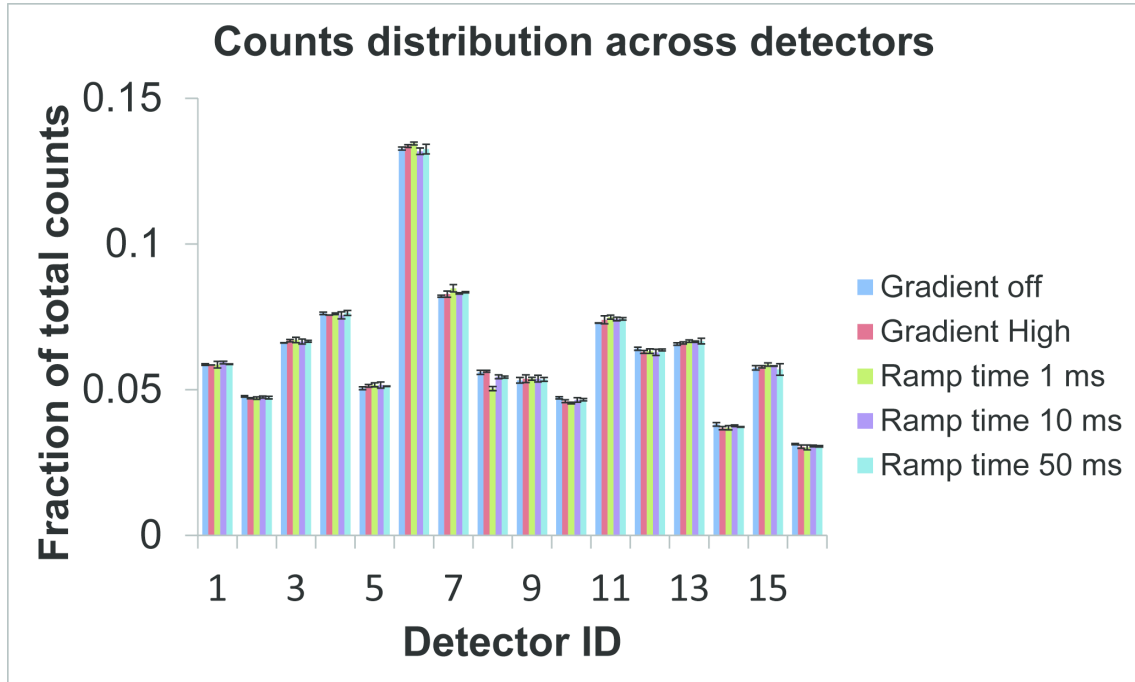


Figure 3.36: MRI gradient effects on count rates for individual detectors. Coincident counts measured from the PET insert were sorted to relevant detector pair (each count was thus counted twice) for each gradient pulsing condition. The count variation across multiple detectors is due to the different amplification gains of individual PSAPDs. The differences between different gradient conditions were generally small (<10%). The greatest count attenuation were observed during rapid risetimes (~1ms). This was most pronounced for detector 8. Error bars are SD.

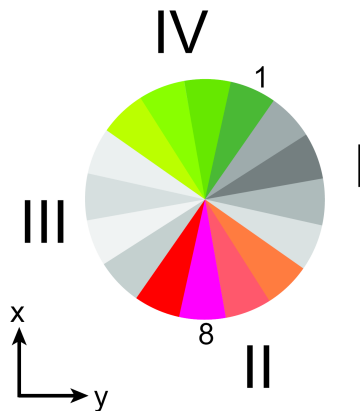


Figure 3.37: Orientation of PET detector modules in MRI. The PET insert was orientated within the MRI as shown for the gradient effect experiments. The axis shows the orientation of the x-y MRI gradients. The location of each detector (numbered clockwise in Arabic numerals and shown by slice wedges) is approximated by the wedges. The locations were split into for quadrants (numbered in Roman numerals and colored) for analysis.

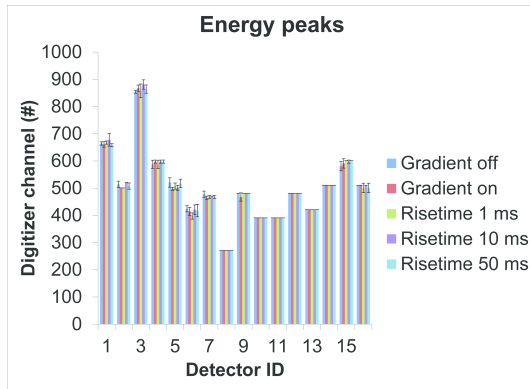
Table 3.11: Count rate differences across different gradient conditions for individual detectors. P-values from one-way ANOVA analysis across different gradient conditions are listed, with significantly different conditions (when applicable) from subsequent multiple comparison analyses.

Detector ID	<i>p-value</i> from ANOVA analysis	Descriptions of significantly different conditions
1	0.4	–
2	0.2	–
3	0.4	–
4	0.52	–
5	0.29	–
6	0.05	–
7	0.02	1 ms risetime was different to all others
8	<0.01	1 ms risetime was different to all others
9	0.9	–
10	0.01	1 ms risetime was different to all others
11	0.09	–
12	0.23	–
13	0.18	–
14	0.07	–
15	0.4	–
16	0.15	–

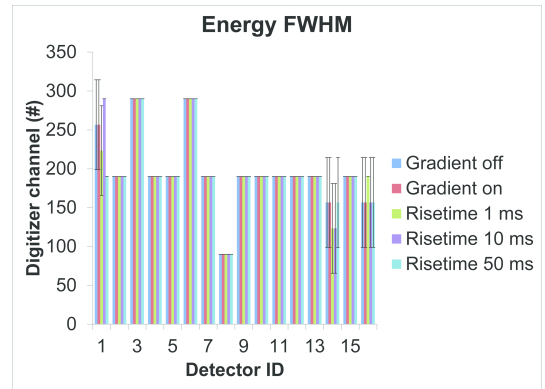
Energy spectra information at different gradient conditions for each detector are shown in figure 3.38. No significant differences for both the peak position and FWHM were observed between all conditions.

3.6.3 Discussion

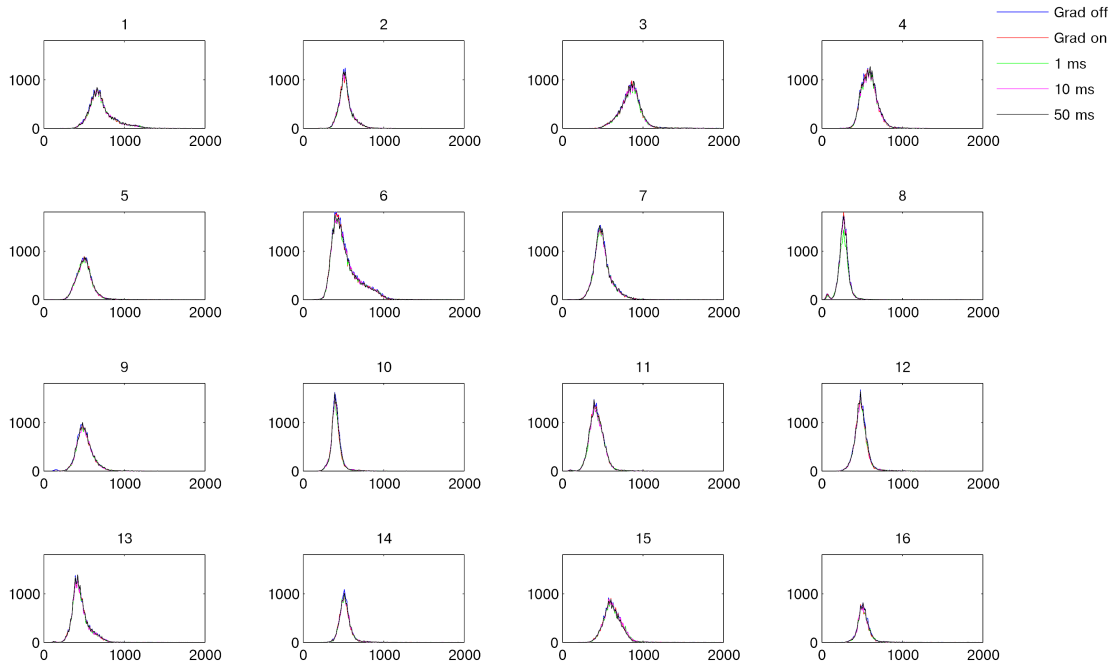
An important consideration in the design of hybrid imaging systems is the presence of interference effects that may hinder each individual imaging modality's performance. Previous studies showed a decrease in count event rates from the PET insert in the presence of running MR-pulse sequences (including gradient switching and RF pulsing) [106]. Further studies using a single PET detector



(a) Energy spectra, peaks, for different gradient conditions



(b) Energy spectra, FWHM, for different gradient conditions.



(c) Energy spectra, for different gradient conditions.

Figure 3.38: Energy spectra for different gradient conditions. Error bars are SD.

module inside the MRI highlighted the effects of gradient strength, switching rates and the location of the detector in relation to the MR gradients toward this decrease [142]. Here, we extended those observations by recording counts from different portions of the gradient waveform. This confirmed that the presence of the MR gradient, whether in a switching or on state, does cause a small but noticeable count attenuation of PET data. Further, increased gradient oscillations showed greater attenuation. These observations are consistent with the fact that greater count attenuation was seen for RARE compared to SE [106] and the fact that sequences with longer TR (lower gradient duty cycle) show less count attenuation.

The interference due to the gradient did not distort the energy spectra, suggesting that the mode of interference is not pure electrical noise. A possible cause for the interference is the presence of eddy currents [142, 211]. However, the exact mechanism of this effect remains unknown and requires further investigation.

Similar investigations with the X and Z gradients, as well as higher (>20%) and longer gradient on states were not pursued because of difficulties with the temperature control of the PET system in these situations. Amplification gains of PSAPDs are temperature dependent [212]. While the MRI and PET temperature controllers can maintain the system's temperature for regular pulse sequences, it is unable to maintain temperature stability for prolonged switching of the gradient. Future PET systems should be more stable [213] and allow further investigations of gradient effects. A corollary of this finding is that the gradient duty cycle for regular pulse sequences are usually low and thus results in a small loss of events.

The findings from this and other studies [211] suggest that strategies can be developed to correct for gradient interference effects. PET data acquired simultaneously with MRI can be gated to different portions of the pulse sequence corresponding to different gradient shapes. Data acquired in the presence of the gradient pulse can either be removed or corrected for count attenuation post acquisition.

RF effects on the PET system were not systematically studied. We observed that RF pulses can cause low energy noise, saturate PET electronics but not affect count rates (consistent with [211]). Prudent shielding and grounding of the cables connecting to the RF coil and leading out of the PET insert, along with proper energy thresholding of PET data eliminated virtually all RF interference

effects. These precautions were adopted for all studies described herein.

In summary, we found that PET count attenuation during pulse sequences is directly related to the presence of the MR gradient. Energy spectra are not degraded during gradient on states, suggesting that counts acquired during these periods do provide useful data provided they are corrected for attenuation effects.

3.7 PET/MRI Informatics Considerations

Multimodal imaging datasets are usually acquired sequentially and integrated posthoc manually. We describe the database and image file generation system that was used in all studies described herein. The system enables almost-automatic integration and processing of multimodal datasets. The setup allows facile analysis of multimodal imaging data individually or together.

3.7.1 Image Generation

MRI and PET images were reconstructed and processed using their native software. To facilitate storage and analysis, images were subsequently converted to the open source NIFTI-1 image format (<http://nifti.nimh.nih.gov/nifti-1>). Subject, timing and imaging parameter information are stored in either the filename or the header file.

3.7.2 Storage

Images are stored on a linux server. The following directory hierarchy is defined:

- Subject
 - Study day
 - * Study number
 - Type of study (PET/ DCE-MRI/ DWI/ MRI anatomical scans etc...)
 - Image files

A screenshot of this hierarchy is shown in figure 3.39.

3.7.3 Integration

The database hierarchy inherently allows different image files acquired from the same study to be linked. However, this information will be lost if images are transferred to another location separately. To account for this, we define a unique identifier that is stored in the NIFTI-1 extension header which permanently links multimodal files from the same study.

The unique identifier is defined by 3 aspects:

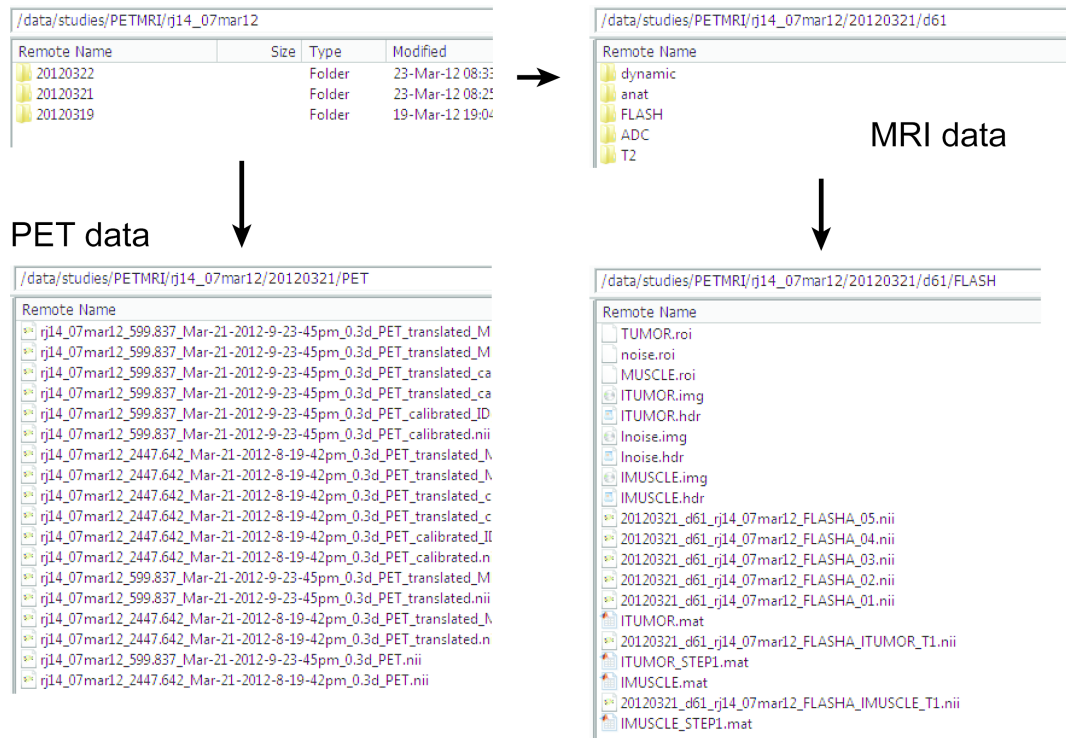


Figure 3.39: PET/MRI database setup. Individual image files (stored as NIFTI-1) are stored according to the subject, date and type of data. An example hierarchy for a typical PET/MRI study subject is shown here. The database is setup on a linux server and implemented using MATLAB.

1. The native modality, which heads the start of the identifier.
2. Associated modalities, which are listed following the native modality information.
3. The time of image acquisition. The timestamp is defined at image acquisition and encoded for all linked modalities during NIFTI-1 file generation.

Code to generate this unique identifier using MATLAB is shown in appendix E.

3.7.4 Discussion

Automatic databasing and integration of multimodal datasets provide several advantages. Firstly, human error during data processing is minimized. Secondly, the introduction of multimodal imaging in recent years is now reaching a stage where complete datasets are now beginning to be sufficiently complex, such that manual analyses are not feasible. Automatic databasing and integration is a step toward approaches that are now commonplace in bioinformatics. The current database setup enables the user to analyse simultaneous PET/MRI data easily in real-time, thus harnessing the advantages offered by the instrumentation. Alternatively, the database also allows the user to analyse large multimodal datasets easily post-acquisition, since the linkage information is already encoded in the hierarchical setup.

Although each imaging modality may have their own proprietary data format, we chose to adopt the open source NIFTI-1 format. The format can be read by a number of free image viewers. The image and header information are also stored as a single file, which is useful for storage and transfer.

A unique identifier to link multimodal images is a compromise between a fully external approach, whereby a spreadsheet is kept of all the data and an fully internal approach, where this spreadsheet is kept inside the image header. The identifier is space efficient and contains all the information that one needs to determine linkage between any two image datasets (type of modalities involved and timing information). The identifier can be stored within the headers of existing data formats and hence will not impede manipulation with current software. A simple plugin can be developed on any software platform to read this identifier and link image datasets together during post-hoc analysis.

In summary, we developed a database system to enable facile processing and integration of

multimodal datasets. This facilitates the analysis of multi-subject, longitudinal imaging studies that are being pursued with the PET/MRI system.